



# Space Weather®



### RESEARCH ARTICLE

10.1029/2023SW003704

#### **Key Points:**

- The storm main phase was characterized by coincident nightside bubble-like ionospheric superdepletion structure (BLISS) and dayside storm-enhanced density (SED)
- The BLISS manifested as a poleward/ westward-streaming channel and extended to ~40 MLAT, corresponding to an APEX height of ~5.000 km
- The SED plume experienced a dynamic variation with the plume intensity being quickly doubled and halved in just a few hours

#### Correspondence to:

E. Aa, aercha@mit.edu

#### Citation:

Aa, E., Zhang, S.-R., Zou, S., Wang, W., Wang, Z., Cai, X., et al. (2024). Significant midlatitude bubble-like ionospheric super-depletion structure (BLISS) and dynamic variation of storm-enhanced density plume during the 23 April 2023 geomagnetic storm. *Space Weather*, 22, e2023SW003704. https://doi.org/10.1029/2023SW003704

Received 6 SEP 2023 Accepted 27 FEB 2024

# Significant Midlatitude Bubble-Like Ionospheric Super-Depletion Structure (BLISS) and Dynamic Variation of Storm-Enhanced Density Plume During the 23 April 2023 Geomagnetic Storm

Ercha Aa<sup>1</sup>, Shun-Rong Zhang<sup>1</sup>, Shasha Zou<sup>2</sup>, Wenbin Wang<sup>3</sup>, Zihan Wang<sup>4</sup>, Xuguang Cai<sup>5</sup>, Philip J. Erickson<sup>1</sup>, and Anthea J. Coster<sup>1</sup>

<sup>1</sup>Haystack Observatory, Massachusetts Institute of Technology, Westford, MA, USA, <sup>2</sup>Department of Climate and Space Sciences and Engineering, University of Michigan, Ann Arbor, MI, USA, <sup>3</sup>High Altitude Observatory, National Center for Atmospheric Research, Boulder, CO, USA, <sup>4</sup>Department of Physics, University of Texas at Arlington, Arlington, TX, USA, <sup>5</sup>Laboratory for Atmospheric and Space Physics, University of Colorado Boulder, Boulder, CO, USA

**Abstract** This paper investigates the midlatitude ionospheric disturbances over the American/Atlantic longitude sector during an intense geomagnetic storm on 23 April 2023. The study utilized a combination of ground-based observations (Global Navigation Satellite System total electron content and ionosonde) along with measurements from multiple satellite missions (GOLD, Swarm, Defense Meteorological Satellite Program, and TIMED/GUVI) to analyze storm-time electrodynamics and neutral dynamics. We found that the storm main phase was characterized by distinct midlatitude ionospheric density gradient structures as follows: (a) In the European-Atlantic longitude sector, a significant midlatitude bubble-like ionospheric super-depletion structure (BLISS) was observed after sunset. This BLISS appeared as a low-density channel extending poleward/westward and reached ~40° geomagnetic latitude, corresponding to an APEX height of ~5,000 km. (b) Coincident with the BLISS, a dynamic storm-enhanced density plume rapidly formed and decayed at local afternoon in the North American sector, with the plume intensity being doubled and halved in just a few hours. (c) The simultaneous occurrence of these strong yet opposite midlatitude gradient structures could be mainly attributed to common key drivers of prompt penetration electric fields and subauroral polarization stream electric fields. This shed light on the important role of storm-time electrodynamic processes in shaping global ionospheric disturbances.

Plain Language Summary The storm-time midlatitude ionosphere is a highly dynamic region that can exhibit much more pronounced electron density gradients and disturbances than expected. The combined data from ground-based and satellite measurements provided valuable insights into the intricate behavior of the midlatitude ionosphere during an intense geomagnetic storm on 23 April 2023. The midlatitude ionosphere was characterized by significant electron density gradient structures, comprising both phenomenal density depletion and exceptional enhancements. Notably, a remarkable band-like ionospheric super-depletion structure was observed in local dusk, which extended to  $\sim 40^{\circ}$  geomagnetic latitude, corresponding to an altitude of  $\sim 5,000$  km above the geomagnetic equator. In contrast, a significant midlatitude ionospheric density enhancement plume appeared simultaneously in local afternoon, which exhibited a dynamic variation with its intensity being quickly doubled and halved in just a few hours. The synchronous occurrence of these striking yet opposing density gradients highlights the importance of electrodynamic effect driven by common key drivers of storm-time perturbed electric fields. This underscores the complex and interconnected nature of the ionospheric response during intense geomagnetic storms.

### 1. Introduction

The storm-time midlatitude ionosphere is a highly dynamic region controlled by various electrodynamic and dynamic processes, which can exhibit significant plasma density gradients that are affected by disturbances originating from both low and high latitudes (Buonsanto, 1999). Ionospheric perturbations in the equatorial latitudes, such as the equatorial plasma bubbles (EPBs), are irregular plasma density depletion structures. EPBs can become more intense during geomagnetically active periods, rising to higher apex altitude and extending toward higher latitudes with enhanced equatorial upward drift driven by eastward prompt penetration electric fields

© 2024. The Authors.

This is an open access article under the terms of the Creative Commons

Attribution License, which permits use, distribution and reproduction in any medium, provided the original work is properly cited.

AA ET AL. 1 of 18

(PPEF) near local dusk (e.g., Abadi et al., 2015; Abdu, 2012; Basu et al., 2007; Greenspan et al., 1991; Kil et al., 2006; Tulasi Ram et al., 2008). Occasionally, these bubble-like ionospheric depletions can extend beyond the equatorial ionization anomaly (EIA) crests and reach the midlatitude region during intense geomagnetic storm period. For example, some studies have reported observations of field-aligned plasma bubbles at 25–30° geomagnetic latitudes (MLAT) around the Arecibo region using all-sky or space-borne imagers (Mendillo et al., 1997; Sousasantos et al., 2023). In another event, super plasma bubbles were detected at ~31° MLAT over Japan using Global Navigation Satellite System (GNSS) total electron content (TEC) measurements (Ma & Maruyama, 2006). Similarly, Foster and Rich (1998) measured a distinct EPB-like ionospheric depletion using the Millstone Hill incoherent scatter radar around 35–37° MLAT. Moreover, recent studies employing coordinated ground-based observations and satellite in-situ measurements have revealed that these bubble-like plasma depletions can form poleward-streaming structures that extend considerably across the midlatitude region, reaching unexpectedly subauroral latitudes of 40–50° MLAT, such as over the European longitude sector (Cherniak & Zakharenkova, 2016; Katamzi-Joseph et al., 2017), Asian-Pacific longitude sector (Aa et al., 2018; Huang et al., 2007; Li et al., 2018), and American longitude sector (e.g., Aa et al., 2019; Chang et al., 2022; Cherniak & Zakharenkova, 2022; Martinis et al., 2015; Sori et al., 2023; Zakharenkova & Cherniak, 2020).

On the other hand, apart from the above-mentioned depletion structure, the storm-time midlatitude ionosphere could also have large-scale density enhancements characterized by significant horizontal gradients, known as storm-enhanced density (SED, Foster, 1993). SED typically refers to a plume-like structure of enhanced ionospheric TEC and electron density (Ne) that elongates along a sunward/poleward direction in the local afternoon sector at subauroral latitudes (e.g., Coster et al., 2007; M. C. Kelley et al., 2004; Zhang & Aa, 2021; Zou et al., 2013). In some cases, the SED plume may convect through the dayside cusp region into the polar cap to form the polar tongue of ionization (Foster et al., 2005). The generation of the SED plume is widely considered to be related to the storm-time eastward penetration electric fields and the equatorward expansion of the highlatitude convection pattern: the reduced chemical recombination, associated with the upward plasma drift to higher altitudes with lower recombination rates, causes electron density enhancements. This effect is further augmented by the TEC/Ne build-up around a zonal flow stagnation region in the afternoon sector, owing to the opposite direction between the westward flow and Earth's corotation (e.g., Heelis et al., 2009; Liu et al., 2016; Thomas et al., 2013; Zou et al., 2014). Moreover, some studies suggest that the formation of the SED plume could be related to the erosion of the outer plasmasphere (Bao et al., 2023; Goldstein et al., 2003). This is associated with the occurrence of the subauroral polarization stream (SAPS, Foster & Burke, 2002), where the horizontal advection of large plasma flux transported by the sunward SAPS flow may serve as an important source of the SED plume (e.g., Aa, Zhang, Wang, et al., 2023; Foster et al., 2007; Foster et al., 2020; Zou et al., 2013). In addition, the storm-induced equatorward neutral wind surge (Balan et al., 2010; Mendillo, 2006), as well as the composition change with the downwelling of neutral species at mid-to-low latitude (Immel et al., 2001; W. Wang et al., 2012), may also contribute to the TEC/Ne enhancements in the SED region. Overall, the generation of the SED plume is a result of multiple processes acting simultaneously.

These storm-induced midlatitude ionospheric density gradients, including both large bubble-like depletion and SED plume, are frequently associated with strong plasma density irregularities and scintillation that can pose significant threats to the performance of GNSS-based systems at midlatitudes (Coster & Skone, 2009; Mrak et al., 2020; Nishimura et al., 2021; Rodrigues et al., 2021). However, our current understanding of these unique gradient structures remains incomplete, and certain critical issues require further investigation:

1. What are the driving mechanisms of the midlatitude Bubble-Like Ionospheric Super-depletion Structure (BLISS)? BLISS is an inclusive term used to encompass different names and observations of the aforementioned midlatitude bubble-like plasma density depletion beyond EIA crests, which will be used thereafter in this manuscript. We assigned the term BLISS to differentiate it from EPBs for three main reasons. (a) Exceptional latitudinal extension: While EPBs are normally observed in the equatorial and low-latitude ionosphere, BLISS demonstrates a more pronounced latitudinal expansion toward higher latitudes, capable of reaching midlatitude and even subauroral latitudes of 40–50° MLAT. This corresponds to an APEX altitude of 5,000+ km above the geomagnetic dip equator. (b) Large westward-tilting morphology: Westward tilt is a nominal morphological feature of EPBs, which frequently extend along the magnetic field-lines and may exhibit a slight backward C-shape with varying, yet small, westward tilt angles of 10–15° (Aa et al., 2020; Kil, 2015; Xiong et al., 2016). However, BLISS can demonstrate a much greater westward-tilting morphology with tilting angle reaching 45° or so, significantly deviating from the magnetic field line orientation (e.g., Aa

AA ET AL. 2 of 18

et al., 2018, 2019). (c) Widespread controversy exists in the scientific community regarding mechanisms that are not easily measurable: The nomenclature BLISS arose due to its underlying mechanism remains widely debated with no definitive consensus. Some studies indicate that BLISS are the latitudinal extension of super EPBs due to the extreme fountain effect driven by PPEF (e.g., Aa et al., 2018; Cherniak & Zakharenkova, 2016, 2022; Katamzi-Joseph et al., 2017; Martinis et al., 2015), while some other studies propose that BLISS are not associated with EPBs but rather represent signatures of medium-scale traveling ionospheric disturbances (Chang et al., 2022; Kil et al., 2016) or midlatitude density irregularities (Nishimura et al., 2021). In addition, some studies suggest that the poleward/westward-streaming shape of BLISS is generated through strong electric fields in the SAPS region (e.g., Aa et al., 2019; Huang et al., 2007; Zakharenkova & Cherniak, 2020). These seemingly conflicting explanations might be attributed to the incomplete spatial/temporal coverage of the unevenly distributed observational data sets, thus demanding an in-depth investigation of the generation mechanisms of BLISS with new data sets and providing the motivation for introducing a new coin.

2. Can SED plume and BLISS be observed simultaneously during a storm, and can they be explained by a common driver? These two phenomena represent strong yet opposite storm-time midlatitude ionospheric density variations, with SED plume and BLISS indicating plasma enhancements and depletion, respectively. However, these two features are often reported and studied separately, despite that both have stream-like shapes with somewhat similar morphology and both tend to occur during storm time. Thus, comprehending the development and evolution of these distinct and potentially related midlatitude ionospheric gradients constitutes an important objective in frontier space weather research.

Therefore, to further address the aforementioned questions, we have conducted a multi-instrument analysis of midlatitude ionospheric disturbances during an intense geomagnetic storm on 23-24 April 2023. This storm marked the largest geomagnetic storm in Solar Cycle 25 to date, with the maximum Kp index reaching 8+. The data sets used in our analysis include ground-based GNSS TEC and ionosonde observations, along with spaceborne measurements from various sources such as the Swarm constellation, Defense Meteorological Satellite Program (DMSP), TIMED (Thermosphere Ionosphere Mesosphere Energetics and Dynamics), and geostationary-orbiting GOLD (Global-scale Observations of the Limb and Disk) mission. Our finds reveal that the storm's early main phase was characterized by two distinct midlatitude plasma density gradient structures, occurring simultaneously in different longitude sectors: (a) In the European-Atlantic longitude sector at local dusk, a significant BLISS phenomenon was observed. It extended in a poleward/westward direction from lowlatitudes toward subauroral latitudes, reaching ~40° MLAT that corresponds to an APEX height of 5,000 km above the dip equator. (b) In the North American longitude sector at local afternoon, a strong SED plume rapidly formed and decayed with density being doubled and halved in merely a few hours. Interestingly, this dayside SED plume appeared almost concurrently with the postsunset BLISS. Therefore, we conduct a comprehensive analysis of the observational evidence for these two distinct features, along with their potential drivers and possible connections. We aim to gain deeper insights into the mechanisms behind these midlatitude ionospheric disturbances during this intense geomagnetic storm.

### 2. Instruments and Data Sets

The ground-based TEC data are generated at the Massachusetts Institute of Technology's Haystack Observatory using 5,000+ worldwide GNSS receivers (Rideout & Coster, 2006; Vierinen et al., 2016). To investigate the storm-time ionospheric variation, we utilize gridded TEC products with a spatial-temporal resolution of 1° (longitude) by 1° (latitude) and 5 min. To understand the distribution and evolution of ionospheric irregularities, we also use the line-of-sight TEC data from all available satellite-receiver pairs to calculate the rate of TEC index (ROTI) (Aa et al., 2019; Pi et al., 1997). ROTI is calculated as the 5-min standard deviation of the time derivative of TEC. Additionally, we use ionosonde measurements from El Arenosillo (37.1°N, 6.7°W) in the European-Atlantic sector to examine the local ionospheric variation related to BLISS.

Besides ground-based data sets, this study incorporates space-borne measurements from four satellite missions: GOLD, Swarm, DMSP, and TIMED. The GOLD instrument is a dual-channel ultraviolet-imaging spectrometer located in a geostationary orbit at 47.5°W longitude, which measures Earth's airglow emissions between 132 and 162 nm through the disk, limb, and stellar occultation with a stationary field-of-view (Eastes et al., 2017). In this study, we use the nighttime disk measurements of OI 135.6 nm emission. These measurements provide continuous images in the local early evening hours, offering insights into the spatial-temporal variations of equatorial and low-latitude ionospheric dynamics from West African to South American longitude sectors with

AA ET AL. 3 of 18

15 min temporal resolution (e.g., Aa et al., 2020, 2022; Aa, Zhang, Liu, et al., 2023; Cai et al., 2021, 2022, 2023; Eastes et al., 2020; Karan et al., 2020). In addition, we use in-situ electron density measurements from the polar-orbiting Swarm B satellite at an altitude of  $\sim$ 500 km. Also, data from the sun-synchronous DMSP F16 and F17 satellites at  $\sim$ 850 km are used, including the electron and ion energy flux data from the precipitating particle sensor as well as ion density and cross-track drift data from the ionospheric plasma monitor sensor. The TIMED satellite carries the Global Ultraviolet Imager (GUVI), which yield daytime thermospheric composition along the satellite track. We use the column density ratio of  $O/N_2$  to monitor storm-time thermospheric composition changes, which is derived from OI 135.6 nm and the  $N_2$  Lyman-Birge-Hopfield emissions (Strickland et al., 1995; Y. Zhang et al., 2004).

### 3. Interplanetary and Geomagnetic Conditions

Figures 1a-1e show the temporal variation of solar wind speed and dynamic pressure, interplanetary magnetic field (IMF) By and Bz components, interplanetary electric field (IEF), Kp index, and the longitudinally symmetric index (SYM-H) during 23-25 April 2023. The solar activity during this time was at a moderate level, with the F10.7 index maintaining between 132 and 136 solar flux unit (sfu, 1 sfu =  $10^{-22}$  W/m<sup>2</sup>/Hz). A full-halo coronal mass ejection (CME) was produced at 18:12 UT on Apr 21 associated with an M1.7-class solar flare eruption from an Active Region 13,283. The CME hit Earth at 17:37 UT on April 23, leading to an intense geomagnetic storm in the following 24 hr. On April 23, the solar wind speed increased dramatically from ~350 km/s at 17 UT to ~700 km/s at 21 UT; the IMF Bz experienced a strong southward excursion during 18-21 UT, with a minimum value of -25 nT at 18:53 UT; the Kp index reached 8+ during 18-21 UT; the SYM-H index exhibited a significant dip, reaching -179 nT at 21:59 UT on Apr 23. The geomagnetic storm sustained on April 24 due to the continued effect of the CME with clear magnetic cloud signature, possibly with some contribution from coronal hole high-speed streams. On April 24, the solar wind speed fluctuated between 550 and 650 km/s; the IMF Bz reached a minimum value of -33 nT at 01:21 UT; the Kp index reach 8 during 03-06 UT; the SYM-H index reached a minimum value of -233 nT at 04:03 UT. This particular geomagnetic storm was the largest one in Solar Cycle 25 to date, which generated some dramatic midlatitude ionospheric density gradients, characterized by both depletion (BLISS) and enhancements (SED plume), as will be further described below.

### 4. Results

Figure 2 shows combined GNSS TEC and GOLD OI 135.6 nm radiance maps with overlapping paths of Swarm B (black) and DMSP F17 (red) at four UTs on 23 April 2023, which provide synoptic views of the mid- and low-latitude ionospheric characteristics in the early main phase of the storm over the African-American-Atlantic longitude sector. The right sub-panels show the corresponding latitudinal profiles of Swarm Ne and DMSP ion drift. Note that we focus on the plasma flow direction and relative change along the orbit in the midlatitude region. We have checked that the DMSP SSIES data at midlatitude ionosphere used in this study exhibited relatively high density ( $>3 \times 10^4$  cm<sup>-3</sup>) with a majority of O+ (>75%), indicating good data quality of reliable results.

At 18:55 UT (Figure 2a), shortly after the IMF Bz reached a southward excursion of -25 nT, distinct EPB signatures of irregular plasma depletion can be observed in Swarm Ne profile in the equatorial region over the African longitude, and the EIA crests are located around 15–20° MLAT over the American-Atlantic longitude in the TEC maps. The DMSP horizontal plasma drift in the low and midlatitude region is eastward with a few hundred m/s, consistent with the typical eastward zonal drift of EPBs near dusk (e.g., Makela, 2006; Martinis et al., 2003). Notably, the DMSP vertical plasma drift in the equatorial and low-latitude region reached ~100 m/s. This indicates a strong storm-time equatorial fountain effect, which was caused by enhanced eastward zonal electric fields likely due to a combination of PPEF and dusktime pre-reversal enhancement (PRE). Such a large upward E×B drift played a key role in increasing the growth rate of the Rayleigh-Taylor instability, thereby effectively facilitating the development of the observed postsunset EPBs (e.g., Abdu, 2012; Basu et al., 2007; Retterer & Roddy, 2014; Sultan, 1996).

At 20:22 UT (Figure 2b), the IMF Bz remained extremely southward around  $-20 \, \mathrm{nT}$  for  $\sim 2.5 \, \mathrm{hr}$ . During this time, clear EPBs signatures were observed in both the GOLD image and the Swarm Ne profile, characterized by strong equatorial plasma bite-outs as low as  $10^3 \, \mathrm{el/cm^3}$ . However, the combined GOLD and TEC map revealed an interesting phenomenon over West Africa: a branch of EPBs exhibited a significant latitudinal extension, cutting

AA ET AL. 4 of 18

15427390, 2024, 3, Downloaded from https://agupubs.onlinelibrary.wiley.com/doi/10.1029/2023SW003704, Wiley Online Library on [29/09/2024]. See the Terms and Conditions (https://agupubs.onlinelibrary.wiley.com/doi/10.1029/2023SW003704, Wiley Online Library on [29/09/2024]. See the Terms and Conditions (https://agupubs.com/doi/10.1029/2023SW003704, Wiley Online Library on [29/09/2024].

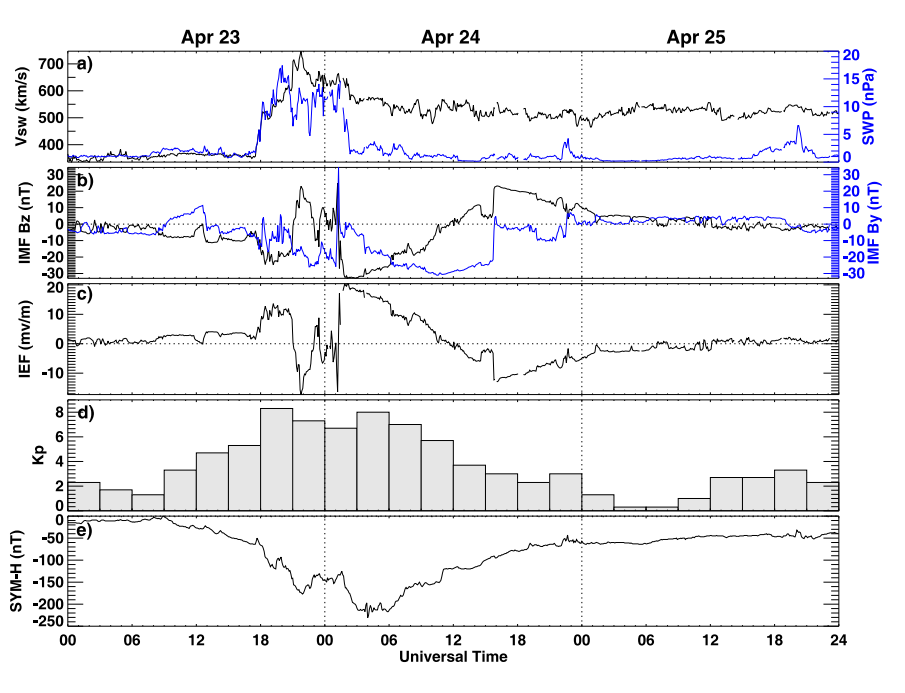


**Figure 1.** Temporal variations of (a) solar wind speed and dynamic pressure, (b) interplanetary magnetic field (IMF) By and Bz components, (c) interplanetary electric field (IEF), (d) Kp index, and (e) longitudinally symmetric index (SYM-H) during April 23–25, 2023.

through the broadened northern EIA crest. This extension formed a band-like depletion channel in a poleward/ westward direction as marked by a black arrow, reaching midlatitude region of 30-40° MLAT. This distinctive depletion channel, as described in the introduction section, is referred to as the BLISS. As observed, the background TEC is 50-60 TECU in the vicinity of BLISS region. Within the BLISS area, the TEC values drop to approximately 20 TECU, signifying a substantial depletion of more than 50%. The GOLD image also reveals a pronounced depletion of 60%-80% within BLISS. Besides its band-like latitudinal extension, one of the unique features of BLISS is that it was located near the transition region between eastward and westward flows, which is different from typical behavior of EPBs with eastward drift. This is evident in the DMSP horizontal plasma drift data (Figure 2b), where the poleward edge of BLISS is co-located with an intense westward plasma drift from about 35° MLAT and above, peaking at ~1 km/s. This suggests signatures of SAPS associated with the equatorward expansion of convection. Defense Meteorological Satellite Program data also indicates strong ion upflows in the topside ionosphere in the SAPS region. Besides the ExB drift driven by PPEF due to sustained southward IMF Bz, the large upward ion drift in the dusk subauroral latitudes could also be related to the Type-1 ion upflow, which is a consequence of enhanced ion-neutral frictional heating associated with fast SAPS flow channels (e.g., Anderson et al., 1991; Erickson et al., 2010; Yeh & Foster, 1990; H. Wang & Lühr, 2013). Additionally, the equatorial and low-latitude ionosphere also experienced large upward drift of a couple hundred m/s, indicating a strong equatorial fountain effect driven by prolonged PPEF. These large westward and upward plasma drift are key characteristics of the storm-time midlatitude ionosphere, in which the significant BLISS was observed.

At 22:10 UT (Figure 2c), the BLISS appeared as multiple parallel dark streaks, cutting through the EIA crests and forming connections between the equatorial trough and the midlatitude trough. Notably, the poleward end of BLISS reached as high as ~40° MLAT, as observed in the GOLD image and Swarm Ne profile. This corresponds to an APEX height of ~5,000 km above the geomagnetic equator if BLISS were caused by latitudinal extension of super EPBs. Such a high-latitude/altitude extension of band-like depletion is much more extended than typical EPBs, which are usually confined within 15–20° MLAT (<1,500 km Apex altitude) (Shiokawa et al., 2004). In addition, the Swarm Ne profile reveals the presence of small-scale irregularities embedded within the depletion. Despite the DMSP path being away from the BLISS region, a noticeable SAPS signature persisted with an intense westward flow at around 45–50°MLAT. At 23:22 UT (Figure 2d), even though Swarm and DMSP had moved further westward away from the depletion region, some remnants of EPBs were still discernible on the eastward

AA ET AL. 5 of 18

1.5427390, 2024, 3, Downloaded from https://agupubs.onlinelibrary.viley.com/doi/10.1029/2023SW003704, Wiley Online Library on [29/09/2024]. See the Terms and Conditions (https://onlinelibrary.viley.com/erms-and-conditions) on Wiley Online Library for rules of use; OA articles are governed by the applicable Creative Communications (https://onlinelibrary.viley.com/erms-and-conditions) on Wiley Online Library for rules of use; OA articles are governed by the applicable Creative Communications (https://onlinelibrary.viley.com/erms-and-conditions) on Wiley Online Library for rules of use; OA articles are governed by the applicable Creative Communications (https://onlinelibrary.viley.com/erms-and-conditions) on Wiley Online Library for rules of use; OA articles are governed by the applicable Creative Communications (https://onlinelibrary.viley.com/erms-and-conditions) on Wiley Online Library for rules of use; OA articles are governed by the applicable Creative Communications (https://onlinelibrary.viley.com/erms-and-conditions) on Wiley Online Library for rules of use; OA articles are governed by the applicable Creative Communications (https://onlinelibrary.viley.com/erms-and-conditions) on Wiley Online Library for rules of use; OA articles are governed by the applicable Creative Communications (https://onlinelibrary.viley.com/erms-and-conditions) on Wiley Online Library for rules of use; OA articles are governed by the applicable Creative Communications (https://onlinelibrary.viley.com/erms-and-conditions) on Wiley Online Library for rules of use; OA articles are governed by the applicable Creative Communications (https://onlinelibrary.viley.com/erms-and-conditions) on Wiley Online Library for rules of use; OA articles are governed by the applicable Creative Communications (https://onlinelibrary.viley.com/erms-and-conditions) on the applicable Creative Communication (https://onlinelibrary.viley.com/erms-and-conditions) on the applicable Creative Communication (https://onlinelibrary.viley.com/erms-and-conditions) on

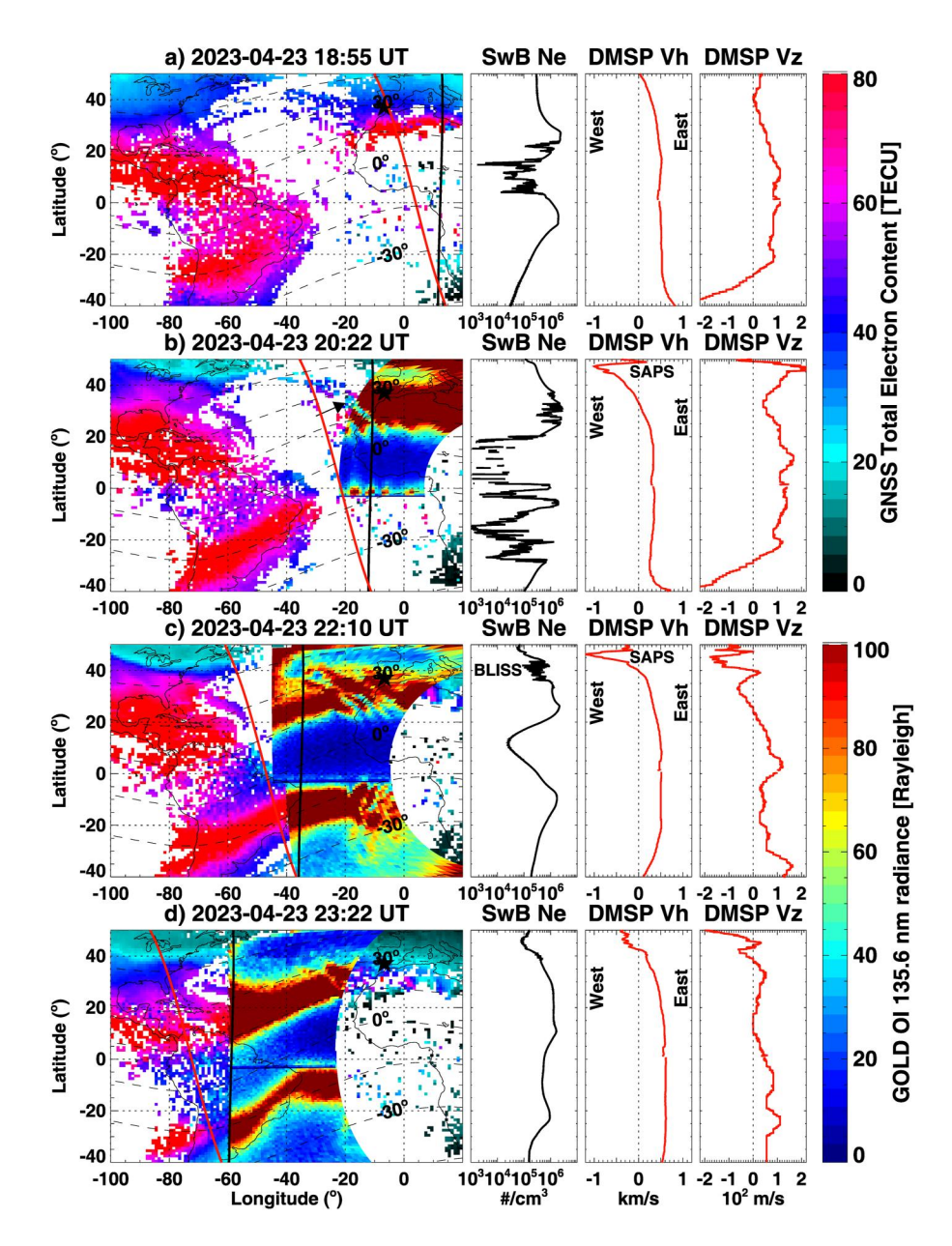


**Figure 2.** (a–d) Combined Global Navigation Satellite System total electron content and GOLD OI 135.6 nm radiance (when available) maps over the African-Atlantic-American longitudes with overlapping Swarm B (black) and Defense Meteorological Satellite Program (DMSP) F17 (red) paths at four UTs between 18:55 UT and 23:22 UT on 23 April 2023. The geomagnetic latitudes with 15° interval are marked by the dashed lines. The black stars mark the location of El Arenosillo ionosonde (37.1°N, 6.7°W). The right sub-panels show the latitudinal profiles of Swarm Ne and DMSP horizontal and vertical ion velocities, respectively.

side of the GOLD image and GNSS TEC in the African longitude sector. Both SAPS and upward plasma drift largely subsided at this time step.

Figure 3 shows the 2-D distribution of TEC ROTI maps, focusing on the midlatitude European-Atlantic region during 18–22 UT on 23 April 2023. These maps illustrate the storm-time development of intense ionospheric irregularities that represented by high ROTI values (0.8–1). The midlatitude ionosphere was subject to intrusions of strong irregularities from both high and low latitudes. On one hand, the zone of strong auroral irregularities expanded considerably equatorward, starting from latitudes higher than 60° MLAT (Figure 3a) at 18 UT and reaching ~45° MLAT (Figures 3d and 3e) at 20 UT. This suggests enhanced auroral precipitation and storm-time high-latitude energy deposition due to strengthened magnetosphere-ionosphere coupling processes

AA ET AL. 6 of 18

15427390, 2024, 3, Downloaded from https://agupubs.onlinelibrary.wiley.com/doi/10.1029/2023SW003704, Wiley Online Library on [29/09/2024]. See the Terms and Cor

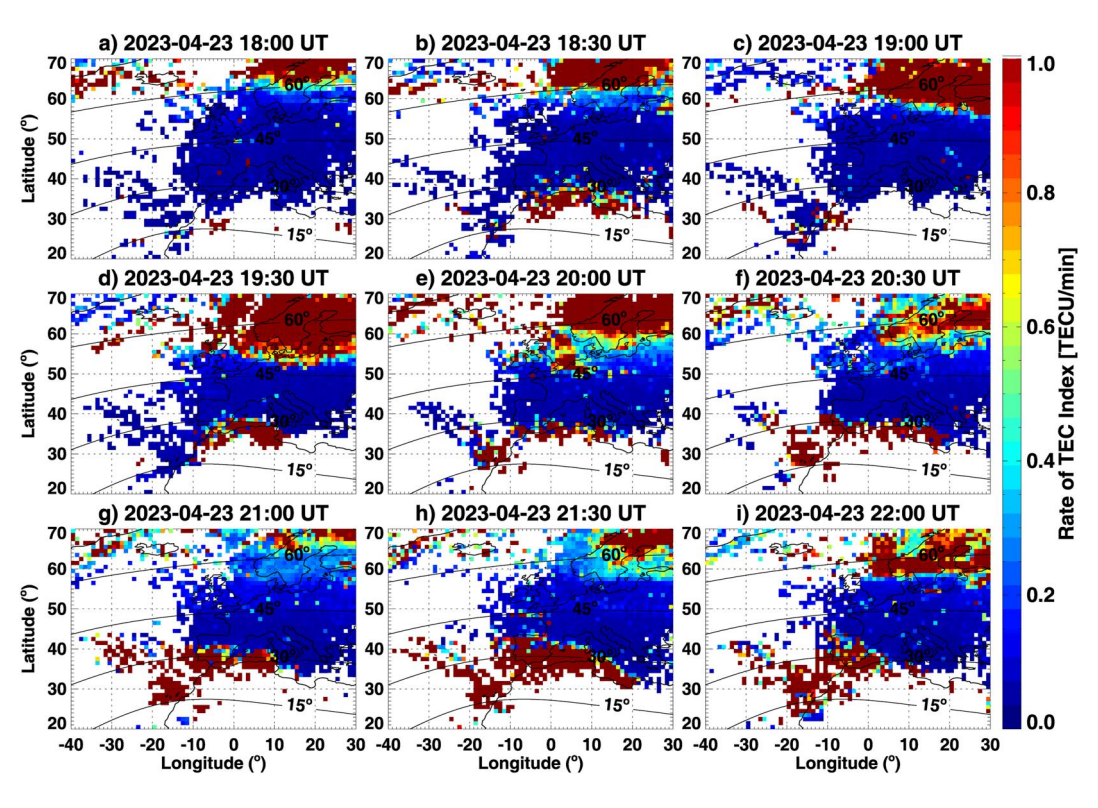


Figure 3. (a-i) ROTI maps showing ionospheric irregularities over the European-Atlantic regions with 30-min interval during 18–22 UT on 23 April 2023.

(Aarons, 1997; Martinis et al., 2015; Mendillo, 2006). On the other side, intense equatorial plasma irregularities were observed over northern Africa that confined to 35° MLAT and lower latitudes. However, during 20:30–22:00 UT, these low-latitude irregularities extended substantially toward the midlatitudes, evolving into northwestward-streaming structures from 15° MLAT to 40° MLAT at around 20–30°W longitude (Figures 3f–3i). This corresponds to an APEX height of ~5,000 km above the dip equator. Such strong midlatitude irregularities with poleward-streaming morphology have also been reported by several studies (e.g., Aa et al., 2018, 2019; Cherniak & Zakharenkova, 2016; Mrak et al., 2020; Zakharenkova & Cherniak, 2020), which are associated with the above-mentioned BLISS as observed by GOLD and TEC in roughly the same location.

The spatial-temporal evolution of auroral and mid-latitude ionospheric irregularities is also examined in Figure 4 using ROTI keogram. Specifically, Figure 4a shows the ROTI keogram as a function of time and latitude along the  $-10^{\circ}$  longitude during 18–24 UT on April 23. As can be seen, intense irregularities with high ROTI values expanded rapidly from auroral zone toward midlatitudes, reaching an equatormost position of 45–48° MLAT at 20:00–20:30 UT. On the other hand, at lower latitudes, strong irregularities were predominately observed in the postsunset sector after 19:30 UT, which quickly extended poleward and reached as high as  $\sim$ 40° MLAT during 21:15–21:30 UT. To further examine the characteristics of irregularities originated from lower latitudes, Figure 4b displays the ROTI keogram as a function of time and longitude along the 40° latitude. This latitude is chosen to focus on the region separated from the strong auroral irregularities at higher latitudes. As seen in the figure, a spread zone of intense ionospheric irregularities appeared shortly after local sunset, most noticeable over the Atlantic longitude sector (-40–0°) during 20–22 UT.

To better analyze the ionospheric disturbances and trace the development of BLISS in a synoptic view, Figure 5 shows 12 consecutive GNSS TEC maps and GOLD nighttime OI 135.6 nm images during 20:10–23:22 UT on April 23. In Figures 5a–5c (20:10–21:10 UT), the available GOLD images from Channel-A of the spectrometer show the northern hemisphere. The postsunset ionosphere exhibited several EPBs, characterized by meridional parallel dark streaks. Among them, a conspicuous band-like depletion channel was observed, cutting through the EIA northern crest and extending poleward/westward from the West African coast toward midlatitude Atlantic. Starting from 21:22 UT, dual-channel images from GOLD became

AA ET AL. 7 of 18

15427390, 2024, 3, Downloaded from https://agupubs.onlinelibrary.wiley.com/doi/10.1029/2023SW003704, Wiley Online Library on [29/09/2024]. See the Terms and Conditions (https://online.com/doi/10.1029/2023SW003704, Wiley Online Library on [29/09/2024]. See the Terms and Conditions (https://online.com/doi/10.1029/2023SW003704, Wiley Online Library on [29/09/2024]. See the Terms and Conditions (https://online.com/doi/10.1029/2023SW003704, Wiley Online Library on [29/09/2024]. See the Terms and Conditions (https://online.com/doi/10.1029/2023SW003704, Wiley Online Library on [29/09/2024]. See the Terms and Conditions (https://online.com/doi/10.1029/2023SW003704, Wiley Online Library on [29/09/2024]. See the Terms and Conditions (https://online.com/doi/10.1029/2023SW003704, Wiley Online Library on [29/09/2024]. See the Terms and Conditions (https://online.com/doi/10.1029/2023SW003704, Wiley Online Library on [29/09/2024]. See the Terms and Conditions (https://online.com/doi/10.1029/2023SW003704, Wiley Online Library on [29/09/2024]. See the Terms and Conditions (https://online.com/doi/10.1029/2023SW003704, Wiley Online Library on [29/09/2024]. See the Terms and Conditions (https://online.com/doi/10.1029/2023SW003704, Wiley Online Library on [29/09/2024]. See the Terms and Conditions (https://online.com/doi/10.1029/2023SW003704, Wiley Online Library on [29/09/2024]. See the Terms and Conditions (https://online.com/doi/10.1029/2023SW003704, Wiley Online Library on [29/09/2024]. See the Terms and Conditions (https://online.com/doi/10.1029/2023SW003704, Wiley Online Library on [29/09/2024]. See the Terms and Conditions (https://online.com/doi/10.1029/2023SW003704, Wiley Online Library on [29/09/2024]. See the Terms and Conditions (https://online.com/doi/10.1029/2023SW003704, Wiley Online Library on [29/09/2024]. See the Terms and Conditions (https://online.com/doi/10.1029/2023SW003704, Wiley Online Library on [29/09/2024]. See the Terms (https://online.com/doi/10.1029/2023SW003704, Wiley Online Library on [29/09/2024]. S

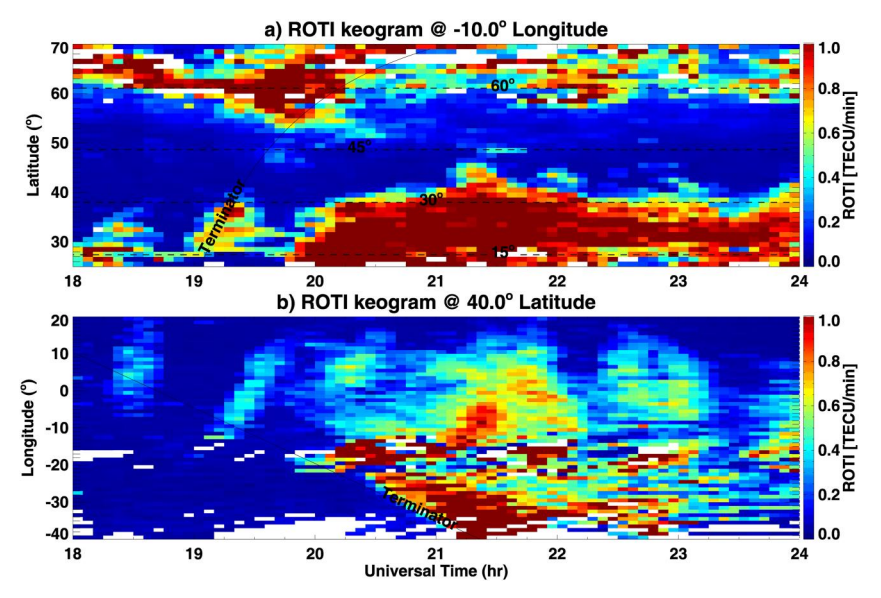


**Figure 4.** ROTI keograms as a function of (a) time and latitude along  $-10^{\circ}$  longitude and (b) time and longitude along  $40^{\circ}$  latitude between 18 and 24 UT on 23 April 2023. The sunset terminator (solid line) and selected geomagnetic latitudes (dashed lines) are also marked.

available, enabling the observation of conjugate BLISS in both hemispheres that displayed a westward-tilt morphology, which is similar to the conjugate EPBs but reached much higher latitudes (Otsuka et al., 2002; Shiokawa et al., 2004). Specifically, these band-like depletion appeared within and beyond EIA crests, reaching as high as ± 40° MLAT in the midlatitude with very large westward-tilting morphology with tilting angles reaching ≥45°, as shown in Figures 5d–5h. As time progressed, starting from 22:40 UT, the BLISS pattern gradually shifted out of GOLD's field of view, although some faint features can still be discerned in Northwest Africa.

In contrast to the significant depletion observed in the postsunset ionosphere, Figure 5 reveals that the dayside midlatitude ionosphere over the North American longitude sector exhibited a positive ionospheric storm phase with a dynamic SED plume. In Figures 5a–5c (20:10–21:10 UT), the GNSS TEC over the continental US showed a significant enhancement of 30%–50%, forming a large electron density base area on the poleward side of the EIA northern crest near the Florida region and the east US coast. Starting from 21:10

UT (Figure 5c), a plume-like TEC enhancement structure originated from the large electron density region at lower midlatitude near east US coast, extending northwestward toward the local noon direction. The SED plume structure was most noticeable during 21:10–22:10 UT (Figures 5c–5g) but was quickly decayed in the following hours (Figures 5h–5l), possibly related to the contracted convection pattern associated with the northward turning of IMF Bz, and/or the negative storm phase that depleted electron densities in middle and high latitudes. This indicates the dynamic nature of the SED plume during the storm period, with significant intensity variation over a relatively shorter time span.

Figures 6a–6d display polar views of TEC overlapping with DMSP F16 cross-track ion drift in the Northern Hemisphere, represented in magnetic local time and geomagnetic latitude (MLAT) coordinates at four different UTs from 17:45–22:45 UT on April 23. In addition, Figures 6e–6h show the corresponding duskside latitudinal variations of electron and ion energy flux, ion density, horizontal ion velocity, and horizontal ion flux between 40 and 70° MLAT. One distinct feature depicted by those plots is the dramatic development and fast decay of the SED plume that associated with dynamic SAPS variation. At 17:45 UT (Figure 6a) and 19:25 UT (Figure 6b), the GNSS TEC in the dayside midlatitude ionospheric over the American sector was around 20–35 TEC unit, and there was a discernible SAPS channel on the equatorward side of auroral precipitation, with peak flow of 966 m/s at ~59° MLAT (Figure 6e) and 875 m/s at ~53° MLAT (Figure 6f).

At 21:05 UT (Figure 6c), a positive ionospheric storm phase occurred in the American longitudinal sector, with midlatitude TEC values being strongly increased by 30%–50% compared to 3 hr before. A significant SED plume emerged in the North American sector, featuring a TEC enhancement channel extending from the high-density midlatitude region in the local afternoon toward the cusp region near noon. Meanwhile, the duskside convection flow and SAPS showed a considerable equatorward shift of 8–10°. In particular, the SAPS channel reached as low as 44–48° MLAT with a strong peak flow of ~1,500 m/s, as marked by the yellow shade in Figure 6g. As time went by, however, this distinct feature of a strong SED plume associated with intense SAPS quickly decayed in the next hour. As shown in Figure 6d at 22:45 UT, the midlatitude ionosphere in the afternoon sector experienced a negative storm phase, with TEC values being significantly reduced by ~30%–50% compared to those at 21:05 UT (Figure 6c). The intensity of SED plume was considerably eroded by ~50%, though some residue of the plume can still be somewhat discerned. Also, Figure 6h shows that SAPS feature disappeared at this time when IMF Bz recovered to positive values. Taken as a whole, such a rapid development and decay of SED plume associated with SAPS in just a few hours is quite dramatic and noteworthy. This phenomenon will be further discussed in the next section to gain a deeper understanding of its mechanisms.

AA ET AL. 8 of 18

15427390, 2024, 3, Downloaded from https://agupub

.wiley.com/doi/10.1029/2023SW003704, Wiley Online Library on [29/09/2024]. See the Terms

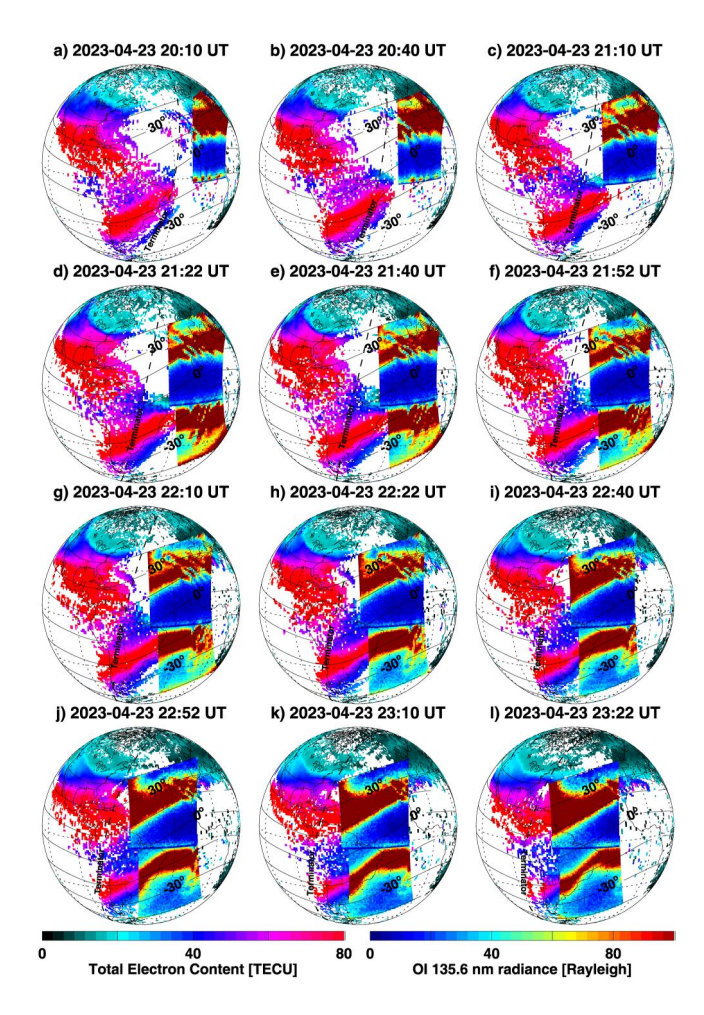


**Figure 5.** (a–l) Temporal variation of combined Global Navigation Satellite System total electron content and GOLD OI 135.6-nm radiance maps between 20:10 UT and 23:22 UT on 23 April 2023. The sunset terminator and geomagnetic latitudes with 15° interval are also shown.

### 5. Discussion

# 5.1. Generation of Bubble-Like Ionospheric Super-Depletion Structure (BLISS)

The postsunset ionosphere over the European-Atlantic longitude sector was characterized by significant BLISS during the storm main phase. The observed BLISS was manifested as a poleward/westward-streaming channel, which presented poleward of EIA crests and extended across midlatitude region reaching as high as  $\sim\!40^\circ$  MLAT during 20–22 UT on April 23. Here, we discuss two potential mechanisms that could be responsible for the formation of BLISS.

### 1. Strong upward plasma drift due to the PPEF effect:

The PPEF is generated by solar wind-magnetosphere dynamo when the electric field, originating from solar wind or the magnetosphere, penetrates almost instantly from the high-latitude to the equatorial ionosphere (M. C. Kelley et al., 2003; Kikuchi et al., 2008; Tsurutani et al., 2008). When the IMF Bz suddenly turns southward, the PPEF exhibits an eastward polarity during the daytime through local dusk, leading to a larger upward E×B drift that uplifts the ionosphere. Specifically, in the dusk sector, the PPEF can overlay on the typical PRE, resulting in an enhanced equatorial fountain effect with a greater plasma upward drift and ambipolar diffusion. The large upward plasma drift favors a large Rayleigh-Taylor instability growth rate, thus promote the development of postsunset plasma bubbles and facilitate their field-aligned extension to higher altitude/latitude locations (e.g., Aggson et al., 1992; Basu et al., 2007; Fejer et al., 1999; Sultan, 1996). In this scenario, the BLISS can be considered as the poleward component of extremely latitudinal-extended plasma bubbles driven by PPEF-induced super fountain (e.g., Aa et al., 2018; Cherniak & Zakharenkova, 2016; Katamzi-Joseph et al., 2017; Martinis et al., 2015). A BLISS event reaching 40° MLAT corresponds to super EPBs rising to an APEX height of ~5,000 km above the dip equator.

To further validate the influence of the PPEF effect on the observed BLISS, we have analyzed data from the midlatitude El Arenosillo ionosonde  $(37.1^{\circ}N, 6.7^{\circ})$  W). This ionosonde locates at the poleward edge of the northern EIA crest of  $\sim 30^{\circ}$  MLAT, in close vicinity of the observed BLISS (Figure 2). Figure 7a

shows the Ne profile and F2-layer peak height (hmF2) at El Arenosillo during 22–23 April 2023. On April 23, hmF2 experienced a significant postsunset rise during 20:30–21:30 UT, reaching an altitude of  $\sim$ 570 km. In comparison, the hmF2 in the same UT on the previous quiet day was much lower at merely  $\sim$ 300 km. Moreover, Figures 7b–7i display a sequence of ionograms illustrating the occurrence of strong range-type spread F starting from 20 UT on April 23. This indicates that large-scale ionospheric irregularities were developed from the bottomside F region due to the increased Rayleigh-Taylor instability. Referring back to Figure 1, the IMF Bz experienced a strong southward excursion of around -20 nT during 18–21 UT on April 23. Therefore, such a coincidental occurrence of strong postsunset F-layer rise and intense spread-F irregularities clearly demonstrates the contribution of PPEF-induced fountain effect to the formation of the observed BLISS.

However, it is worth noting that there are significant morphological differences between EPBs and BLISS. For example, Figure 8a shows a GOLD nighttime partial disk image on 04 December 2019. The equatorial dark streaks highlighted by yellowing dotted lines represent the optical signature of EPBs. In comparison, Figures 8b–8d present three GNSS TEC maps, highlighting BLISS examples indicated by white dotted lines during three strong storms on 08 September 2017, 28 May 2017, and 26 August 2018, respectively. As described in the Introduction section and shown in Figure 8, observations indicate that EPBs are predominantly located within the equatorial and low-latitude regions, which extend along the magnetic field lines with only small tilt angles. In contrast, BLISS demonstrates a more pronounced latitudinal expansion, capable of reaching midlatitude and

AA ET AL. 9 of 18

15427990, 2024, 3, Downloaded from https://agupubs.onlinelibrary.wiley.com/doi/10.1029/2023SW003704, Wiley Online Library on [2909/2024]. See the Terms and Conditions (https://onlinelibrary.wiley.com/terms-and-conditions) on Wiley Online Library for rules of use; OA articles are governed by the applicable Creative Commons License

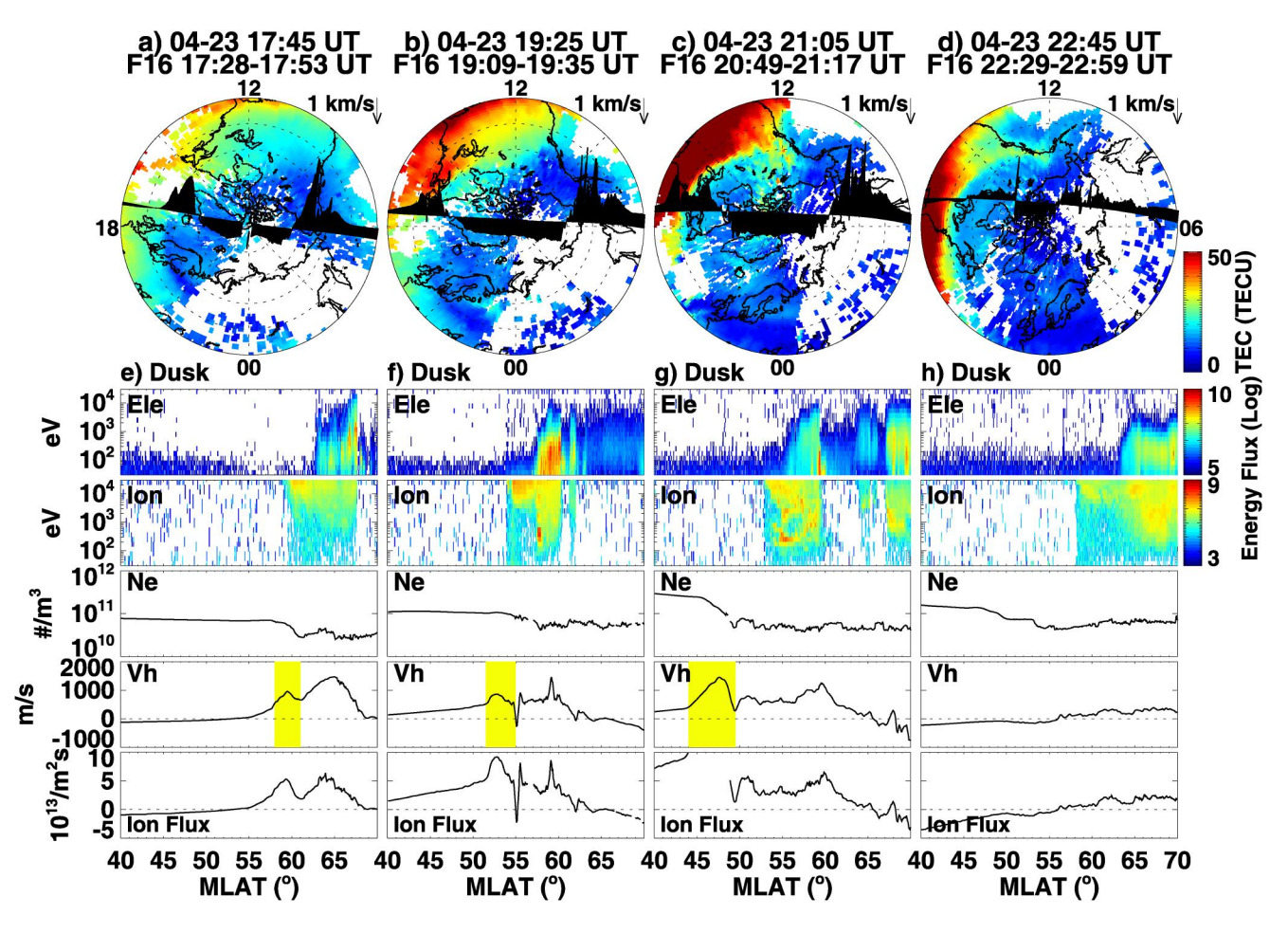


Figure 6. (a–d) Northern Hemisphere polar view of total electron content in the magnetic local time and geomagnetic latitude coordinates, overplotted with Defense Meteorological Satellite Program F16 satellite horizontal ion velocities at four UT intervals during 17:28-22:59 UT on 23 April 2023. Concentric dashed circles are plotted in  $10^{\circ}$  intervals with the outermost one representing  $40^{\circ}$  MLAT. (e–h) The corresponding duskside latitudinal profiles of electron energy flux, ion energy flux, electron density, horizontal cross-track ion drift (positive = sunward), and horizontal ion flux (Ne × Vh) respectively. Yellow shades mark the subauroral polarization stream signature.

subauroral latitudes of 40–50° MLAT. Furthermore, the observed BLISS exhibits a significantly greater westward-tilting morphology than EPBs, with a tilting angle reaching approximately 45° at its poleward end, deviating significantly from the orientation of magnetic field lines. The pronounced poleward-extension and severe westward-tilting feature of BLISS can hardly be explained merely using traditional EPB theorems. It is probable that other midlatitude/subauroral processes also played a role in generating BLISS.

### 2. SAPS electric fields and associated polarization electric fields.

Previous studies have revealed that this westward-tilted shape of bubble-like depletion is caused by the latitudinal/altitudinal velocity shear in the ionospheric zonal plasma flow (Kil et al., 2009; Makela & Kelley, 2003). In our study, Figures 2b and 2c show that the poleward part of BLISS was co-located with the equatorward edge of intense SAPS, and there was an clear latitudinal variation in zonal plasma flow velocity. The zonal plasma flow in the vicinity of BLISS reversed from eastward to westward around 35° MLAT and considerably increased to a few hundred m/s at ~40° MLAT, eventually reaching km/s scales at the SAPS peak near ~47° MLAT. Thus, such a large zonal flow shear with velocity increasing from lower to higher latitudes, which was driven by the equatorward expansion of SAPS electric field, could give rise to the westward-tilt shape of BLISS in the midlatitude region (Aa et al., 2019; Zakharenkova & Cherniak, 2020). Moreover, GOLD images in Figure 2 show that the tilted BLISS was situated between areas with enhanced OI 135.6 nm brightness, indicating the presence of high-density regions on both sides of the depletion. Examples of BLISS in GNSS TEC (Figure 8) also reveal similar structures, where the depletion channel is sandwiched between high-density regions. Some studies have indicated

AA ET AL. 10 of 18

15427390, 2024, 3, Downloaded from https://agupubs.onlinelibrary.wiley.com/doi/10.1029/2023SW003704, Wiley Online Library on [29/09/2024]. See the Terms and Conditions (https://onlinelibrary.wiley

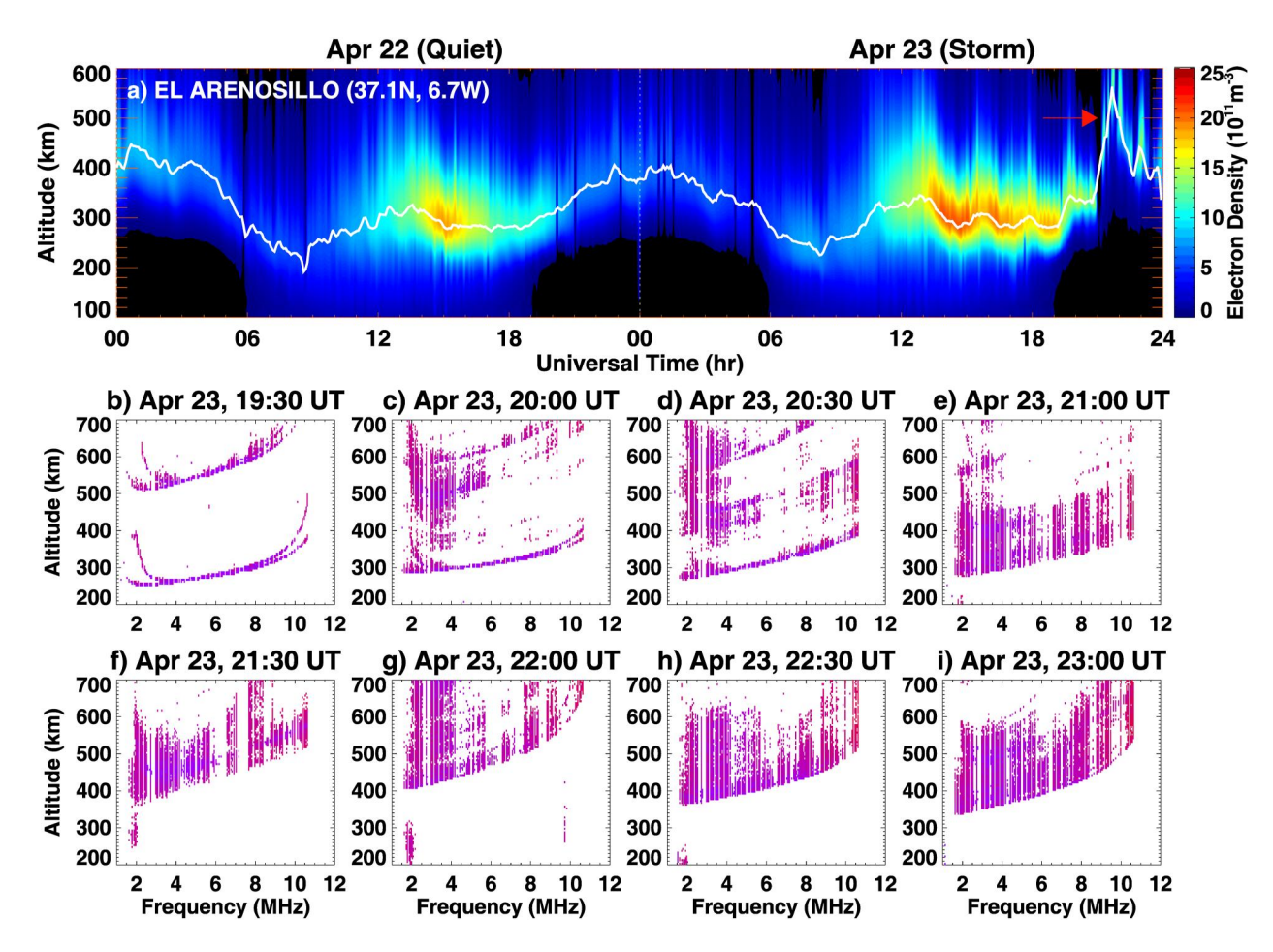


Figure 7. El Arenosillo ionosonde measurements: (a) electron density profile and F2-layer peak height (hmF2) during 22–23 April 2023. The red arrow marks significant storm-time postsunset F-layer rise. (b–i) Sequence of ionograms showing the occurrence of spread-F during 19:30–23:00 UT on 23 April 2023.

that the presence of such sandwiched density gradient structures at midlatitude ionosphere is likely associated with SAPS and polarization electric fields (I. J. Kelley et al., 2023; S.-R. Zhang et al., 2022).

Specifically, Figure 9 shows a schematic diagram illustrating the generation mechanism of polarization electric fields in the Northern Hemisphere. The BLISS region with low Ne is shaded in gray, while regions with high Ne on both sides of BLISS are shaded in yellow. In the midlatitude F-region, the Pedersen current can be expressed as  $J_p = \Sigma_p(E_0 + U \times B)$ , where  $E_0$  represents the external electric field, U is the meridional neutral wind speed, and B is the geomagnetic field. In the current storm-time case, according to the above-mentioned analysis, the midlatitude E<sub>0</sub> is likely dominated by poleward SAPS electric fields plus some contribution from eastward PPEF, thus should be predominantly in the poleward/northeastward direction. Considering that the observed BLISS event occurred in the early phase of the storm, the effect of U is assumed to be much smaller than that of  $E_0$ , as the wind-induced disturbance dynamo is expected to be more significant during the storm recovery phase (Blanc & Richmond, 1980). Thus,  $I_p$  should have the same direction as  $E_0$ . To maintain current continuity of  $I_p$  in the vicinity of BLISS, polarization electric fields  $E_p$  are induced orthogonal to the BLISS direction:  $E_p$  is northeastward in the BLISS region with low Ne (conductivity) and southwestward in regions of high Ne (conductivity) (I. J. Kelley et al., 2023; S.-R. Zhang et al., 2022). Therefore, the direction of E × B drifts induced by the polarization electric fields is expected to be predominantly northwestward (southeastward) within the depletion (enhancement) region, boosting the poleward/westward low-density plasma transportation of BLISS toward higher latitudes. This tilted morphology of BLISS could be the reason why it was sometimes regarded as medium-scale TIDs (Chang et al., 2022; Kil et al., 2016), as typical nighttime medium-scale TIDs also exhibit characteristics of westward-tilted wavefronts similar to BLISS. However, the propagation direction of the nighttime medium-scale TIDs is perpendicular to their wavefronts, which is typically westward/southwestward in the Northern Hemisphere (S.-R.

AA ET AL. 11 of 18

15427390, 2024, 3, Downloaded from https://agupubs.onlinelibrary.wiley.com/doi/10.1029/2023SW003704, Wiley Online Library on [29/09/2024]. See the Terms and Conditions (https://onlinelibrary.wiley.com/terms

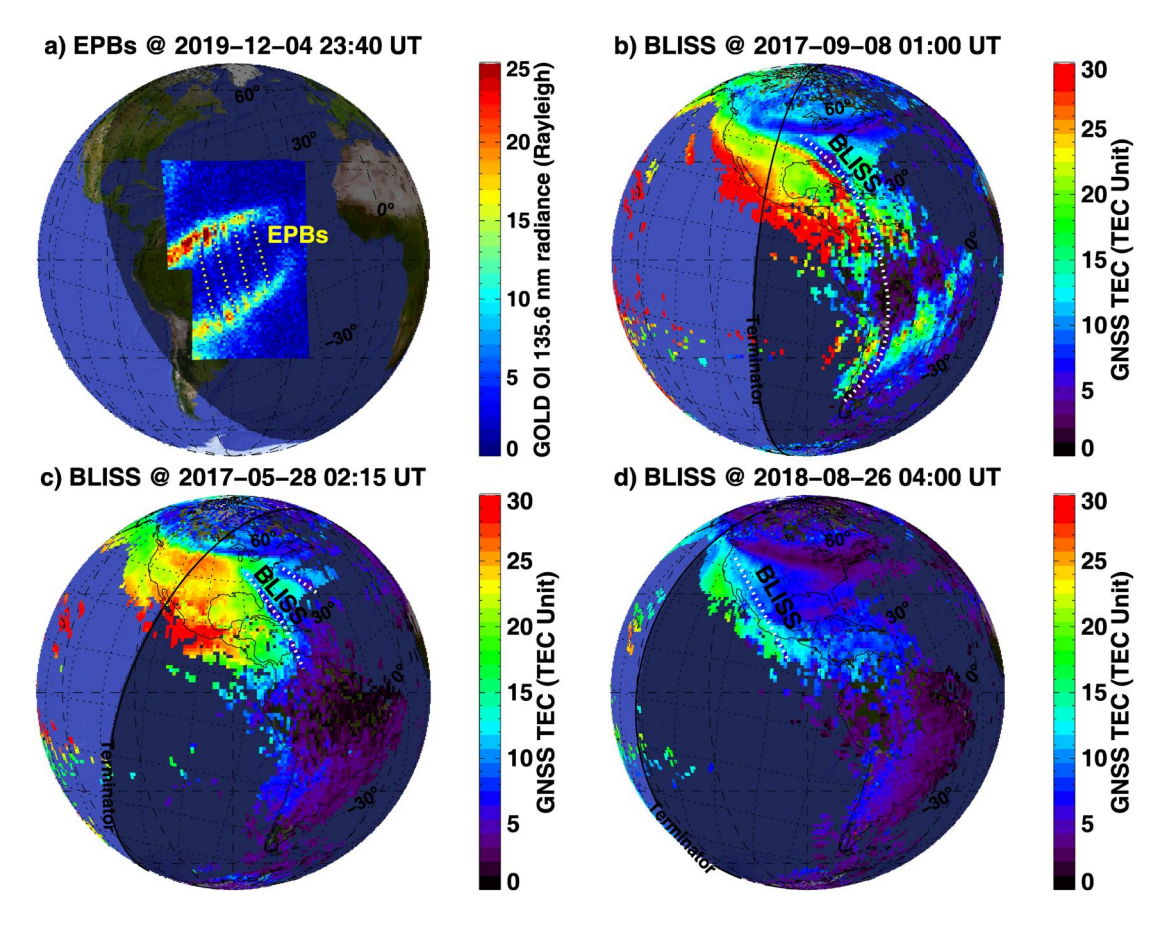


**Figure 8.** (a) GOLD nighttime partial disk image of OI 135.6 nm radiance at 23:40 UT on 04 December 2019. The yellow dotted lines indicate equatorial plasma bubbles. (b–d) Global Navigation Satellite System total electron content maps showing Bubble-Like Ionospheric Super-depletion Structure examples (white dotted lines) on 08 September 2017, 28 May 2017, and 26 August 2018, respectively. Zonal and meridional black dotted lines represent selective geomagnetic latitudes and magnetic field lines, respectively.

Zhang et al., 2019; S.-R. Zhang et al., 2022). This is different from the poleward streaming direction of the depletion channel of BLISS.

In conclusion, the formation of BLISS is likely a result of the complex interplay between multiple ionospheric processes with both mechanisms being involved. For example, if the high-altitude super bubble can reach 5,000 km APEX height above the dip equator under the rising background ionosphere, it could be observed by equatorial orbiting satellite at low L shells. A few previous studies have reported that the field-aligned plasma depletion can extend to at least 3,500–4,000 km in the equatorial plane (Burke et al., 1979; Mendillo et al., 2005). In addition, Obana et al. (2019) observed severe electron density depletion at L=1.6-1.7 domain in the plasmasphere due to long-lasting penetration electric fields. These observations are consistent with our first explanation that high-altitude/latitude EPB/ESF structures can indeed intrude into the midlatitude region under strong PPEF condition. On the other hand, some studies using Super Dual Auroral Radar Network (SuperDARN) and GNSS TEC measurements have observed polarities switching of plasma velocities between midlatitude MSTID-like electron density crests and troughs under background SAPS electric fields, indicating the presence of polarization electric fields and associated electrodynamic/Perkins instability processes (I. J. Kelley et al., 2023; S.-R. Zhang et al., 2022). These observations lend support to our second explanation. Understanding the relative importance of these drivers and other potential mechanisms remains an open issue, which requires future studies with updated data sets and improved modeling capabilities to validate and refine these theories.

### 5.2. Dynamic Development and Decay of SED Plume

In the dayside midlatitude ionosphere over the North American sector, a dynamic SED plume variation was observed: the SED plume appeared almost simultaneously with the postsunset BLISS during 20–22 UT and then

AA ET AL. 12 of 18

15427390, 2024, 3, Downloaded from https://agupubs.onlinelibrary.wiley.com/doi/10.1029/2023SW003704, Wiley Online Library on [29/09/2024]. See the Terms and Conditions (https://onlinelibrary.wiley.com/doi/10.1029/2023SW003704, Wiley Online Library on [29/09/2024]. See the Terms and Conditions (https://onlinelibrary.wiley.com/doi/10.1029/2023SW003704, Wiley Online Library on [29/09/2024]. See the Terms and Conditions (https://onlinelibrary.wiley.com/doi/10.1029/2023SW003704, Wiley Online Library on [29/09/2024]. See the Terms and Conditions (https://onlinelibrary.wiley.com/doi/10.1029/2023SW003704, Wiley Online Library on [29/09/2024]. See the Terms and Conditions (https://onlinelibrary.wiley.com/doi/10.1029/2023SW003704, Wiley.com/doi/10.1029/2023SW003704, Wiley.com/doi/10.10

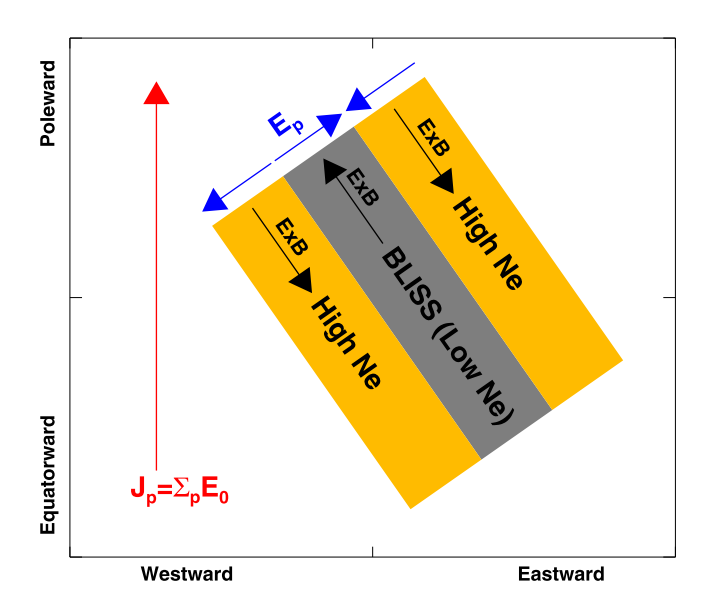


**Figure 9.** A schematic figure illustrating the generation of local polarization electric fields in the vicinity of Bubble-Like Ionospheric Super-depletion Structure (BLISS). The BLISS regions of low Ne is shaded in gray, and regions with high Ne on both sides of BLISS are shaded in yellow.  $J_p$  is the Pedersen current (red arrow).  $E_0$  is the background ionospheric electric field.  $E_p$  is the polarization electric field (blue arrows).

rapidly decayed in the following 1-2 hr with intensity being reduced by ~50%. As part of the positive ionospheric storm phase, the development of SED plume was primarily caused by a large upward plasma drift driven by the strong PPEF mentioned earlier. This uplifted the ionosphere to a higher altitude with lower recombination rate leading to the electron density enhancement (Heelis et al., 2009). In addition, Figures 6b and 6c show that the development of SED plume was preceded/accompanied by the equatorward expansion and intensification of SAPS. Figure 6d displays that the decay of the SED plume was associated with the contraction of convection pattern and the diminish of SAPS after the northward turning of IMF Bz. Such a synchronous variation suggests that convection and SAPS played an important role in the evolution of the SED plume. The bottom panels of Figures 6f and 6g show that the latitudinal profiles of sunward ion flux had a noticeable subauroral enhancement in the region where SAPS overlapped with the poleward edge of the SED base region. This observation suggests that SAPS could transport vast amount of plasma from later local times toward noon via the horizontal advection, potentially contributing to the higher densities in the SED plume (Aa, Zhang, Wang, et al., 2023; Foster et al., 2007; Vlasov et al., 2003; Zou et al., 2013).

The rapid decay of the SED plume on hourly time scales, as depicted in Figure 6d, was likely associated with the contraction of convection pattern and the diminish of SAPS after the northward turning of IMF Bz. Moreover, the decay of the SED might be partially ascribed to the negative storm effect caused by neutral composition change, where  $O/N_2$  ratio is reduced at mid-to-

high latitudes due to atmospheric upwelling of nitrogen-rich air through constant pressure surfaces in the high-latitude region and transported toward lower latitudes (Aa et al., 2021; Fuller-Rowell et al., 1994; Prölss, 2008; Z. Wang et al., 2021; Zhai et al., 2023). Figure 10 shows the daytime TIMED/GUVI O/N<sub>2</sub> global interpolated map on 23 April, overlapping with the trajectories of satellite orbits where the measurements were made. Figure 10b displays the averaged background reference O/N<sub>2</sub> map, calculated using three quiet-day (Kp < 3) data before the storm. Figure 10c shows the delta O/N<sub>2</sub>, obtained by subtracting the reference values from storm-day values. As observed, Figure 10c illustrates that the blue zone of reduced O/N<sub>2</sub> extended from the auroral region to midlatitudes in both hemispheres after the storm onset at ~17:30 UT. In the Northern Hemisphere, the most noticeable O/N<sub>2</sub> reduction of 15%–30% occurred over the North American sector where the SED plume was observed, as the satellite happened to fly over this longitude sector during 18–24 UT on April 23. It can be deduced from Figure 6 that the composition change effect is less effective during the early stages of the storm, as the ionosphere has already been raised to high altitudes by PPEF. However, this composition effect took the advantage from ~22 UT after the subside of PPEF due to northward turning of IMF Bz and descending of the ionosphere, and caused strong negative storm in the midlatitude ionosphere, leading to the rapid erosion of the SED plume.

### 6. Conclusions

In this paper, we have investigated midlatitude ionospheric disturbances over the American/Atlantic longitude sector during the early main phase of an intense geomagnetic storm on 23 April 2023. Our study utilized a range of observational data from multiple instrument, including ground-based GNSS TEC and ionosonde data, as well as space-borne observations from GOLD, Swarm, DMSP, TIMED/GUVI. The main results and findings are summarized as follows.

1. In the European-Atlantic longitude sector, the postsunset midlatitude ionosphere exhibited a distinct BLISS in the storm early main phase during 20–22 UT on April 23. This BLISS appeared as a poleward/westward-streaming channel that extended to ~40° MLAT, corresponding to an APEX height of ~5,000 km above the dip equator. The generation mechanisms of BLISS could be mainly attributed to significant electrodynamic effects, involving substantial altitudinal uplift driven by PPEF, as well as the influence of strong SAPS electric fields and associated polarization electric fields.

AA ET AL. 13 of 18

15427990, 2024, 3, Downloaded from https://agupubs.onlinelibrary.wiley.com/doi/10.1029/2023SW003704, Wiley Online Library on [2909/2024]. See the Terms and Conditions (https://onlinelibrary.wiley.com/terms-and-conditions) on Wiley Online Library for rules of use; OA articles are governed by the applicable Creative Commons License

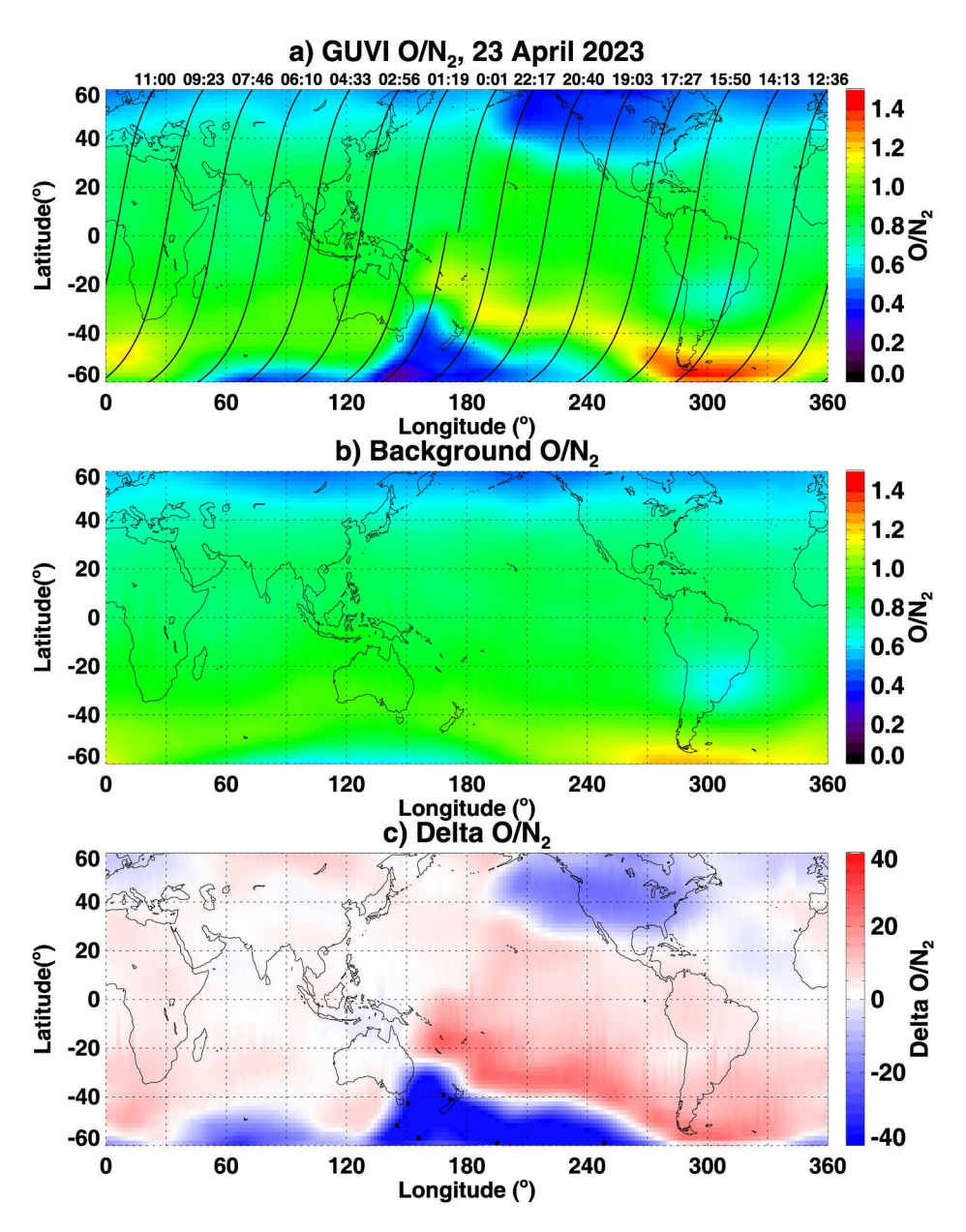


**Figure 10.** (a) GUVI  $O/N_2$  interpolation map on 23 April 2023. The TIMED satellite orbits are marked with black lines, and the UTs when the satellite crossed  $60^{\circ}$  latitude are labels at the top axis. (b) Quiet-time background reference  $O/N_2$  map. (c) Delta  $O/N_2$  map.

2. In the North American longitude sector, the dayside midlatitude ionosphere was characterized by a rapid development and decay of SED plume. The SED plume appeared simultaneously with the postsunset BLISS during 20–22 UT, but it quickly decayed with the plume intensity being largely reduced by ~50% in the subsequent 1–2 hr after the northward turning of IMF Bz. Such a dynamic variation in the SED strength could be primarily attributed to the rapid changes in the IMF direction, which greatly impact the global convection pattern and consequently the geospace plume, along with possible contributions from the thermospheric composition change.

The uniqueness of this storm event is the simultaneous appearance of strongly opposite midlatitude ionospheric gradients, with a notable depletion (BLISS) in the postsunset sector but a concurrent enhancement (SED plume) in the afternoon sector. These distinct but different density gradients were simultaneously driven by common key

AA ET AL. 14 of 18



## **Space Weather**

10.1029/2023SW003704

drivers of PPEF and SAPS electric fields. This synchronous response indicates a significant impact of storm-time electrodynamic processes on the global ionosphere.

### **Data Availability Statement**

GNSS TEC and the DMSP SSIES and SSJ data are provided through Madrigal distributed data system (2023) (http://cedar.openmadrigal.org/) by MIT Haystack Observatory. GOLD data are available at Global-scale Observations of the Limb and Disk (2023) (https://gold.cs.ucf.edu/data/). The solar wind and geophysical parameters data are acquired from NASA/GSFC's Space Physics Data Facility's OMNIWeb service (2023) (https://cdaweb.gsfc.nasa.gov/) and Kyoto world data center for Geomagnetism (2023) (http://wdc.kugi.kyoto-u.ac.jp/). The ionosonde data are provided by the University of Massachusetts Lowell DIDB database of Global Ionospheric Radio Observatory (2023) (https://giro.uml.edu/didbase/scaled.php). Swarm data are provided by European Space Agency (2023) (https://swarm-diss.eo.esa.int/).

### Acknowledgments References

We acknowledge NSF awards AGS-

PHY-2028125, and NSFC41974184.

80NSSC21K1310, 80NSSC21K1775,

FA9559-16-1-0364, and ONR Grant N00014-17-1-2186 and N00014-22-1-

2284. Data for the TEC processing is

80NSSC19K0834, 80NSSC20K1785, and

80GSFC22CA011, AFOSR MURI Project

provided from the following organizations:

The Crustal Dynamics Data Information

System (CDDIS), the Scripps Orbit and

Permanent Array Center (SOPAC), the

(CORS), the EUREF Permanent GNSS

Continuously Operating Reference System

network (EPN), the University NAVSTAR Consortium (UNAVCO), Institut

Geographique National in France (IGN),

Monitoring (RBMC), National Geodetic

Estatistica, RAMSAC CORS of Instituto

Geografico Nacional de la Republica

Argentina, Arecibo Observatory, Low-

Latitude Ionospheric Sensor Network

Canadian High Arctic Ionospheric

Network, Centro di Ricerche

(LISN), Topcon Positioning Systems, Inc.,

Sismologiche, Systeme d'Observation du

permanent, GeoNet-the official source of

geological hazard information for New

Zealand, GNSS Reference Networks.

Niveau des Eaux Littorales (SONEL),

RENAG: REseau NAtional GPS

Finnish Meteorological Institute,

SWEPOS-Sweden.

Survey, Instituto Brasileiro de Geografia e

the Brazilian Network for Continuous

NASA support 80NSSC22K0171,

1952737, AGS-2033787, AGS-2149698,

- Aa, E., Huang, W., Liu, S., Ridley, A., Zou, S., Shi, L., et al. (2018). Midlatitude plasma bubbles over China and adjacent areas during a magnetic storm on 8 September 2017. Space Weather, 16(3), 321–331. https://doi.org/10.1002/2017SW001776
- Aa, E., Zhang, S., Erickson, P. J., Coster, A. J., Goncharenko, L. P., Varney, R. H., & Eastes, R. (2021). Salient midlatitude ionosphere-ther-mosphere disturbances associated with SAPS during a minor but geo-effective storm at deep solar minimum. *Journal of Geophysical Research: Space Physics*, 126(7), e2021JA029509. https://doi.org/10.1029/2021ja029509
- Aa, E., Zhang, S.-R., Liu, G., Eastes, R. W., Wang, W., Karan, D. K., et al. (2023). Statistical analysis of equatorial plasma bubbles climatology and multi-day periodicity using GOLD observations. *Geophysical Research Letters*, 50(8), e2023GL103510. https://doi.org/10.1029/2023GL103510
- Aa, E., Zhang, S.-R., Wang, W., Erickson, P. J., & Coster, A. J. (2023). Multiple longitude sector storm-enhanced density (SED) and long-lasting subauroral polarization stream (SAPS) during the 26–28 February 2023 geomagnetic storm. *Journal of Geophysical Research: Space Physics*, 128(9), e2023JA031815. https://doi.org/10.1029/2023JA031815
- Aa, E., Zhang, S.-R., Wang, W., Erickson, P. J., Qian, L., Eastes, R., et al. (2022). Pronounced suppression and X-pattern merging of equatorial ionization anomalies after the 2022 Tonga volcano eruption. *Journal of Geophysical Research: Space Physics*, 127(6), e30527. https://doi.org/10.1029/2022JA030527
- Aa, E., Zou, S., Eastes, R., Karan, D. K., Zhang, S.-R., Erickson, P. J., & Coster, A. J. (2020). Coordinated ground-based and space-based observations of equatorial plasma bubbles. *Journal of Geophysical Research: Space Physics*, 125(1), e27569. https://doi.org/10.1029/20191A027569
- Aa, E., Zou, S., Ridley, A., Zhang, S., Coster, A. J., Erickson, P. J., et al. (2019). Merging of storm time midlatitude traveling ionospheric disturbances and equatorial plasma bubbles. *Space Weather*, 17(2), 285–298. https://doi.org/10.1029/2018SW002101
- Aarons, J. (1997). Global positioning system phase fluctuations at auroral latitudes. *Journal of Geophysical Research*, 102(A8), 17219–17232. https://doi.org/10.1029/97JA01118
- Abadi, P., Otsuka, Y., & Tsugawa, T. (2015). Effects of pre-reversal enhancement of E × B drift on the latitudinal extension of plasma bubble in Southeast Asia. *Earth Planets and Space*, 67(1), 74. https://doi.org/10.1186/s40623-015-0246-7
- Abdu, M. A. (2012). Equatorial spread F/plasma bubble irregularities under storm time disturbance electric fields. *Journal of Atmospheric and Solar-Terrestrial Physics*, 75, 44–56. https://doi.org/10.1016/j.jastp.2011.04.024
- Aggson, T. L., Burke, W. J., Maynard, N. C., Hanson, W. B., Anderson, P. C., Slavin, J. A., et al. (1992). Equatorial bubbles updrafting at supersonic speeds. *Journal of Geophysical Research*, 97(A6), 8581–8590. https://doi.org/10.1029/92JA00644
- Anderson, P. C., Heelis, R. A., & Hanson, W. B. (1991). The ionospheric signatures of rapid subauroral ion drifts. *Journal of Geophysical Research*, 96(A4), 5785–5792, https://doi.org/10.1029/90JA02651
- Balan, N., Shiokawa, K., Otsuka, Y., Kikuchi, T., Vijaya Lekshmi, D., Kawamura, S., et al. (2010). A physical mechanism of positive ionospheric storms at low latitudes and midlatitudes. *Journal of Geophysical Research*, 115(A2), A02304. https://doi.org/10.1029/2009JA014515
- Bao, S., Wang, W., Sorathia, K., Merkin, V., Toffoletto, F., Lin, D., et al. (2023). The relation among the ring current, subauroral polarization stream, and the geospace plume: MAGE simulation of the 31 March 2001 super storm. *Journal of Geophysical Research: Space Physics*, 128(12), e2023JA031923. https://doi.org/10.1029/2023JA031923
- Basu, S., Basu, S., Rich, F. J., Groves, K. M., MacKenzie, E., Coker, C., et al. (2007). Response of the equatorial ionosphere at dusk to penetration electric fields during intense magnetic storms. *Journal of Geophysical Research*, 112(A8), A08308. https://doi.org/10.1029/2006JA012192
  Blanc, M., & Richmond, A. D. (1980). The ionospheric disturbance dynamo. *Journal of Geophysical Research*, 85(A4), 1669–1686. https://doi.org/10.1029/JA085iA04p01669
- Buonsanto, M. J. (1999). Ionospheric storms—A review. Space Science Reviews, 88(3/4), 563–601. https://doi.org/10.1023/A:1005107532631

  Burke, W. J., Donatelli, D. E., Sagalyn, R. C., & Kelley, M. C. (1979). Low density regions observed at high altitudes and their connection with equatorial spread F. Planetary and Space Science, 27(5), 593–601. https://doi.org/10.1016/0032-0633(79)90157-0
- Cai, X., Burns, A. G., Wang, W., Qian, L., Liu, J., Solomon, S. C., et al. (2021). Observation of Postsunset OI 135.6 nm radiance enhancement over South America by the GOLD mission. *Journal of Geophysical Research: Space Physics*, 126(2), e28108. https://doi.org/10.1029/ 2020JA028108
- Cai, X., Qian, L., Wang, W., McInerney, J. M., Liu, H.-L., & Eastes, R. W. (2022). Investigation of the post-sunset extra electron density peak poleward of the equatorial ionization anomaly southern crest. *Journal of Geophysical Research: Space Physics*, 127(9). e2022JA030755. https://doi.org/10.1029/2022JA030755
- Cai, X., Wang, W., Eastes, R. W., Qian, L., Pedatella, N. M., Aa, E., et al. (2023). Equatorial ionization anomaly discontinuity observed by GOLD, COSMIC-2, and ground-based GPS receivers' network. *Geophysical Research Letters*, 50(10), e2023GL102994. https://doi.org/10.1029/2023GL102994

AA ET AL. 15 of 18

15427390, 2024, 3, Downloaded from

.com/doi/10.1029/2023SW003704, Wiley Online Library on [29/09/2024]. See the

- Chang, H., Kil, H., Sun, A. K., Zhang, S.-R., & Lee, J. (2022). Ionospheric disturbances in low- and midlatitudes during the geomagnetic storm on 26 August 2018. *Journal of Geophysical Research: Space Physics*, 127(2), e2021JA029879. https://doi.org/10.1029/2021JA029879
- Cherniak, I., & Zakharenkova, I. (2016). First observations of super plasma bubbles in Europe. Geophysical Research Letters, 43(21), 11137–11145. https://doi.org/10.1002/2016GL071421
- Cherniak, I., & Zakharenkova, I. (2022). Development of the storm-induced ionospheric irregularities at equatorial and middle latitudes during the 25–26 August 2018 geomagnetic storm. Space Weather, 20(2), e2021SW002891. https://doi.org/10.1029/2021SW002891
- Coster, A. J., Colerico, M. J., Foster, J. C., Rideout, W., & Rich, F. (2007). Longitude sector comparisons of storm enhanced density. Geophysical Research Letters, 34(18), L18105. https://doi.org/10.1029/2007GL030682
- Coster, A. J., & Skone, S. (2009). Monitoring storm-enhanced density using IGS reference station data. *Journal of Geodesy*, 83(3–4), 345–351. https://doi.org/10.1007/s00190-008-0272-3
- Eastes, R. W., McClintock, W. E., Burns, A. G., Anderson, D. N., Andersson, L., Aryal, S., et al. (2020). Initial observations by the GOLD mission. *Journal of Geophysical Research: Space Physics*, 125(7), e27823. https://doi.org/10.1029/2020JA027823
- Eastes, R. W., McClintock, W. E., Burns, A. G., Anderson, D. N., Anderson, L., Codrescu, M., et al. (2017). The global-scale observations of the limb and disk (GOLD) mission. Space Science Reviews, 212(1–2), 383–408. https://doi.org/10.1007/s11214-017-0392-2
- Erickson, P. J., Goncharenko, L. P., Nicolls, M. J., Ruohoniemi, M., & Kelley, M. C. (2010). Dynamics of North American sector ionospheric and thermospheric response during the November 2004 superstorm. *Journal of Atmospheric and Solar-Terrestrial Physics*, 72(4), 292–301. https://doi.org/10.1016/j.jastp.2009.04.001
- European Space Agency. (2023). Swarm data [Dataset]. https://swarm-diss.eo.esa.int/
- Fejer, B. G., Scherliess, L., & de Paula, E. R. (1999). Effects of the vertical plasma drift velocity on the generation and evolution of equatorial spread F. *Journal of Geophysical Research*, 104(A9), 19859–19870. https://doi.org/10.1029/1999JA900271
- Foster, J. C. (1993). Storm time plasma transport at middle and high latitudes. *Journal of Geophysical Research*, 98(A2), 1675–1690. https://doi.org/10.1029/92JA02032
- Foster, J. C., & Burke, W. J. (2002). SAPS: A new categorization for sub-auroral electric fields. EOS Transactions, 83(36), 393–394. https://doi.org/10.1029/2002E0000289
- Foster, J. C., Coster, A. J., Erickson, P. J., Holt, J. M., Lind, F. D., Rideout, W., et al. (2005). Multiradar observations of the polar tongue of
- ionization. Journal of Geophysical Research, 110(A9), A09S31. https://doi.org/10.1029/2004JA010928
  Foster, J. C., Erickson, P. J., Walsh, B. M., Wygant, J. R., Coster, A. J., & Zhang, Q.-H. (2020). Multi-point observations of the geospace plume. In
- Dayside magnetosphere interactions (pp. 243–264). American Geophysical Union (AGU). https://doi.org/10.1002/9781119509592.ch14
  Foster, J. C., & Rich, F. J. (1998). Prompt midlatitude electric field effects during severe geomagnetic storms. Journal of Geophysical Research, 103(A11), 26367, 26377. https://doi.org/10.1002/971A03057
- 103(A11), 26367–26372. https://doi.org/10.1029/97JA03057
  Foster, J. C., Rideout, W., Sandel, B., Forrester, W. T., & Rich, F. J. (2007). On the relationship of SAPS to storm-enhanced density. Journal of
- Atmospheric and Solar-Terrestrial Physics, 69(3), 303–313. https://doi.org/10.1016/j.jastp.2006.07.021
- Fuller-Rowell, T. J., Codrescu, M. V., Moffett, R. J., & Quegan, S. (1994). Response of the thermosphere and ionosphere to geomagnetic storms. Journal of Geophysical Research, 99(A3), 3893–3914. https://doi.org/10.1029/93JA02015
- Global-scale Observations of the Limb and Disk. (2023). Global-scale observations of the limb and disk data [Dataset]. https://gold.cs.ucf.edu/data/
- Goldstein, J., Sandel, B. R., Hairston, M. R., & Reiff, P. H. (2003). Control of plasmaspheric dynamics by both convection and sub-auroral polarization stream. Geophysical Research Letters, 30(24), 2243. https://doi.org/10.1029/2003GL018390
- Greenspan, M. E., Rasmussen, C. E., Burke, W. J., & Abdu, M. A. (1991). Equatorial density depletions observed at 840 km during the great magnetic storm of March 1989. *Journal of Geophysical Research*, 96(A8), 13931–13942. https://doi.org/10.1029/91JA01264
- Heelis, R. A., Sojka, J. J., David, M., & Schunk, R. W. (2009). Storm time density enhancements in the middle-latitude dayside ionosphere. Journal of Geophysical Research, 114(A3), A03315. https://doi.org/10.1029/2008JA013690
- Huang, C.-S., Foster, J. C., & Sahai, Y. (2007). Significant depletions of the ionospheric plasma density at middle latitudes: A possible signature of equatorial spread F bubbles near the plasmapause. *Journal of Geophysical Research*, 112(A5), A05315. https://doi.org/10.1029/2007JA012307
   Immel, T. J., Crowley, G., Craven, J. D., & Roble, R. G. (2001). Dayside enhancements of thermospheric O/N<sub>2</sub> following magnetic storm onset.
- Journal of Geophysical Research, 106(A8), 15471–15488. https://doi.org/10.1029/2000JA000096
- Karan, D. K., Daniell, R. E., England, S. L., Martinis, C. R., Eastes, R. W., Burns, A. G., & McClintock, W. E. (2020). First zonal drift velocity measurement of equatorial plasma bubbles (EPBs) from a geostationary orbit using GOLD data. *Journal of Geophysical Research: Space Physics*, 125(9), e28173. https://doi.org/10.1029/2020JA028173
- Katamzi-Joseph, Z. T., Habarulema, J. B., & Hernández-Pajares, M. (2017). Midlatitude postsunset plasma bubbles observed over Europe during intense storms in April 2000 and 2001. Space Weather, 15(9), 1177–1190. https://doi.org/10.1002/2017SW001674
- Kelley, I. J., Kunduri, B. S. R., Baker, J. B. H., Ruohoniemi, J. M., & Shepherd, S. G. (2023). Storm time electrified MSTIDs observed over mid-latitude North America. *Journal of Geophysical Research: Space Physics*, 128(3), e2022JA031115. https://doi.org/10.1029/2022JA031115
- Kelley, M. C., Makela, J. J., Chau, J. L., & Nicolls, M. J. (2003). Penetration of the solar wind electric field into the magnetosphere/ionosphere system. Geophysical Research Letters, 30(4), 1158. https://doi.org/10.1029/2002GL016321
- Kelley, M. C., Vlasov, M. N., Foster, J. C., & Coster, A. J. (2004). A quantitative explanation for the phenomenon known as storm-enhanced density. Geophysical Research Letters, 31(19), L19809. https://doi.org/10.1029/2004GL020875
- Kikuchi, T., Hashimoto, K. K., & Nozaki, K. (2008). Penetration of magnetospheric electric fields to the equator during a geomagnetic storm. Journal of Geophysical Research, 113(A6), A06214. https://doi.org/10.1029/2007JA012628
- Kil, H. (2015). The morphology of equatorial plasma bubbles—A review. Journal of Astronomy and Space Sciences, 32(1), 13–19. https://doi.org/10.5140/JASS.2015.32.1.13
- Kil, H., Heelis, R. A., Paxton, L. J., & Oh, S.-J. (2009). Formation of a plasma depletion shell in the equatorial ionosphere. *Journal of Geophysical Research*, 114(A11), A11302. https://doi.org/10.1029/2009JA014369
- Kil, H., Miller, E. S., Jee, G., Kwak, Y.-S., Zhang, Y., & Nishioka, M. (2016). Comment on "The night when the auroral and equatorial ionospheres converged" by Martinis, C., J. Baumgardner, M. Mendillo, J. Wroten, A. Coster, and L. Paxton. *Journal of Geophysical Research: Space Physics*, 121(10), 10599–10607. https://doi.org/10.1002/2016JA022662
- Kil, H., Paxton, L. J., Su, S.-Y., Zhang, Y., & Yeh, H. (2006). Characteristics of the storm-induced big bubbles (SIBBs). *Journal of Geophysical Research*, 111(A10), A10308. https://doi.org/10.1029/2006JA011743
- Kyoto world data center for Geomagnetism. (2023). Geomagnetic data [Dataset]. http://wdc.kugi.kyoto-u.ac.jp/
- Li, G., Ning, B., Wang, C., Abdu, M. A., Otsuka, Y., Yamamoto, M., et al. (2018). Storm-enhanced development of postsunset equatorial plasma bubbles around the meridian 120°E/60°W on 7-8 September 2017. *Journal of Geophysical Research: Space Physics*, 123(9), 7985–7998. https://doi.org/10.1029/2018JA025871

AA ET AL. 16 of 18

10.1029/2023SW003704



## **Space Weather**

- Liu, J., Wang, W., Burns, A., Solomon, S. C., Zhang, S., Zhang, Y., & Huang, C. (2016). Relative importance of horizontal and vertical transports to the formation of ionospheric storm-enhanced density and polar tongue of ionization. *Journal of Geophysical Research: Space Physics*, 121(8), 8121–8133. https://doi.org/10.1002/2016JA022882
- Ma, G., & Maruyama, T. (2006). A super bubble detected by dense GPS network at east Asian longitudes. Geophysical Research Letters, 33(21), L21103. https://doi.org/10.1029/2006GL027512
- Madrigal distributed data system. (2023). Data from the CEDAR Madrigal database [Dataset]. http://cedar.openmadrigal.org/
- Makela, J. J. (2006). A review of imaging low-latitude ionospheric irregularity processes. *Journal of Atmospheric and Solar-Terrestrial Physics*, 68(13), 1441–1458. https://doi.org/10.1016/j.jastp.2005.04.014
- Makela, J. J., & Kelley, M. C. (2003). Field-aligned 777.4-nm composite airglow images of equatorial plasma depletions. *Geophysical Research Letters*, 30(8), 1442. https://doi.org/10.1029/2003GL017106
- Martinis, C., Baumgardner, J., Mendillo, M., Wroten, J., Coster, A., & Paxton, L. (2015). The night when the auroral and equatorial ionospheres converged. *Journal of Geophysical Research: Space Physics*, 120(9), 8085–8095. https://doi.org/10.1002/2015JA021555
- Martinis, C., Eccles, J. V., Baumgardner, J., Manzano, J., & Mendillo, M. (2003). Latitude dependence of zonal plasma drifts obtained from dual-site airglow observations. *Journal of Geophysical Research*, 108(A3), 1129. https://doi.org/10.1029/2002JA009462
- Mendillo, M. (2006). Storms in the ionosphere: Patterns and processes for total electron content. *Reviews of Geophysics*, 44(4), RG4001. https://doi.org/10.1029/2005RG000193
- Mendillo, M., Baumgardner, J., Nottingham, D., Aarons, J., Reinisch, B., Scali, J., & Kelley, M. (1997). Investigations of thermospheric-ionospheric dynamics with 6300-Å images from the Arecibo Observatory. *Journal of Geophysical Research*, 102(A4), 7331–7344. https://doi.org/10.1029/96JA02786
- Mendillo, M., Zesta, E., Shodhan, S., Sultan, P. J., Doe, R., Sahai, Y., & Baumgardner, J. (2005). Observations and modeling of the coupled latitude-altitude patterns of equatorial plasma depletions. *Journal of Geophysical Research*, 110(A9), A09303. https://doi.org/10.1029/ 2005IA011157
- Mrak, S., Semeter, J., Nishimura, Y., Rodrigues, F. S., Coster, A. J., & Groves, K. (2020). Leveraging geodetic GPS receivers for ionospheric scintillation science. *Radio Science*, 55(11), e2020RS007131. https://doi.org/10.1029/2020RS007131
- NASA/GSFC's Space Physics Data Facility's OMNIWeb service. (2023). Solar wind and geophysical parameters data [Dataset]. https://cdaweb.gsfc.nasa.gov/
- Nishimura, Y., Mrak, S., Semeter, J. L., Coster, A. J., Jayachandran, P. T., Groves, K. M., et al. (2021). Evolution of mid-latitude density irregularities and scintillation in North America during the 7–8 September 2017 storm. *Journal of Geophysical Research: Space Physics*, 126(6), e29192. https://doi.org/10.1029/2021JA029192
- Obana, Y., Maruyama, N., Shinbori, A., Hashimoto, K. K., Fedrizzi, M., Nosé, M., et al. (2019). Response of the ionosphere-plasmasphere coupling to the September 2017 storm: What erodes the plasmasphere so severely? *Space Weather*, 17(6), 861–876. https://doi.org/10.1029/2019SW002168
- Otsuka, Y., Shiokawa, K., Ogawa, T., & Wilkinson, P. (2002). Geomagnetic conjugate observations of equatorial airglow depletions. *Geophysical Research Letters*, 29(15), 1753. https://doi.org/10.1029/2002GL015347
- Pi, X., Mannucci, A. J., Lindqwister, U. J., & Ho, C. M. (1997). Monitoring of global ionospheric irregularities using the Worldwide GPS Network. Geophysical Research Letters, 24(18), 2283–2286. https://doi.org/10.1029/97GL02273
- Prölss, G. W. (2008). Ionospheric storms at mid-latitude: A short review (Vol. 181, pp. 9–24). Washington DC American Geophysical Union Geophysical Monograph Series. https://doi.org/10.1029/181GM03
- Retterer, J. M., & Roddy, P. (2014). Faith in a seed: On the origins of equatorial plasma bubbles. *Annales Geophysicae*, 32(5), 485–498. https://doi.org/10.5194/angeo-32-485-2014
- Rideout, W., & Coster, A. (2006). Automated gps processing for global total electron content data. GPS Solutions, 10(3), 219–228. https://doi.org/10.1007/s10291-006-0029-5
- Rodrigues, F. S., Socola, J. G., Moraes, A. O., Martinis, C., & Hickey, D. A. (2021). On the properties of and ionospheric conditions associated with a mid-latitude scintillation event observed over southern United States. Space Weather, 19(6), e2021SW002744. https://doi.org/10.1029/2021SW002744
- Shiokawa, K., Otsuka, Y., Ogawa, T., & Wilkinson, P. (2004). Time evolution of high-altitude plasma bubbles imaged at geomagnetic conjugate points. *Annales Geophysicae*, 22(9), 3137–3143. https://doi.org/10.5194/angeo-22-3137-2004
- Sori, T., Shinbori, A., Otsuka, Y., Nishioka, M., Perwitasari, S., & Nishitani, N. (2023). First detection of midlatitude plasma bubble by SuperDARN during a geomagnetic storm on May 27 and 28, 2017. *Journal of Geophysical Research: Space Physics*, 128(4), e2022JA031157. https://doi.org/10.1029/2022JA031157
- Sousasantos, J., Gomez Socola, J., Rodrigues, F. S., Eastes, R. W., Brum, C. G. M., & Terra, P. (2023). Severe L-band scintillation over low-to-mid latitudes caused by an extreme equatorial plasma bubble: Joint observations from ground-based monitors and GOLD. *Earth Planets and Space*, 75(1), 41. https://doi.org/10.1186/s40623-023-01797-5
- Strickland, D. J., Evans, J. S., & Paxton, L. J. (1995). Satellite remote sensing of thermospheric O/N<sub>2</sub> and solar EUV. 1. Theory. *Journal of Geophysical Research*, 100(A7), 12217–12226. https://doi.org/10.1029/95JA00574
- Sultan, P. J. (1996). Linear theory and modeling of the Rayleigh-Taylor instability leading to the occurrence of equatorial spread F. Journal of Geophysical Research, 101(A12), 26875–26892. https://doi.org/10.1029/96JA00682
- Thomas, E. G., Baker, J. B. H., Ruohoniemi, J. M., Clausen, L. B. N., Coster, A. J., Foster, J. C., & Erickson, P. J. (2013). Direct observations of the role of convection electric field in the formation of a polar tongue of ionization from storm enhanced density. *Journal of Geophysical Research: Space Physics*, 118(3), 1180–1189. https://doi.org/10.1002/jgra.50116
- Tsurutani, B. T., Verkhoglyadova, O. P., Mannucci, A. J., Saito, A., Araki, T., Yumoto, K., et al. (2008). Prompt penetration electric fields (PPEFs) and their ionospheric effects during the great magnetic storm of 30-31 October 2003. *Journal of Geophysical Research*, 113(A5), A05311. https://doi.org/10.1029/2007JA012879
- Tulasi Ram, S., Rama Rao, P. V. S., Prasad, D. S. V. V. D., Niranjan, K., Gopi Krishna, S., Sridharan, R., & Ravindran, S. (2008). Local time dependent response of postsunset ESF during geomagnetic storms. *Journal of Geophysical Research*, 113(A7), A07310. https://doi.org/10.1029/2007JA012922
- University of Massachusetts Lowell DIDB database of Global Ionospheric Radio Observatory. (2023). Ionosonde data [Dataset]. https://giro.uml.edu/didbase/scaled.php
- Vierinen, J., Coster, A. J., Rideout, W. C., Erickson, P. J., & Norberg, J. (2016). Statistical framework for estimating GNSS bias. Atmospheric Measurement Techniques, 9(3), 1303–1312. https://doi.org/10.5194/amt-9-1303-2016

AA ET AL. 17 of 18



## **Space Weather**

- 10.1029/2023SW003704
- Vlasov, M., Kelley, M. C., & Kil, H. (2003). Analysis of ground-based and satellite observations of F-region behavior during the great magnetic storm of July 15, 2000. *Journal of Atmospheric and Solar-Terrestrial Physics*, 65(11–13), 1223–1234. https://doi.org/10.1016/j.jastp.2003. 08.012
- Wang, H., & Lühr, H. (2013). Seasonal variation of the ion upflow in the topside ionosphere during SAPS (subauroral polarization stream) periods. *Annales Geophysicae*, 31(9), 1521–1534. https://doi.org/10.5194/angeo-31-1521-2013
- Wang, W., Talaat, E. R., Burns, A. G., Emery, B., Hsieh, S.-Y., Lei, J., & Xu, J. (2012). Thermosphere and ionosphere response to subauroral polarization streams (SAPS): Model simulations. *Journal of Geophysical Research*, 117(A7), A07301. https://doi.org/10.1029/2012JA017656
- Wang, Z., Zou, S., Liu, L., Ren, J., & Aa, E. (2021). Hemispheric asymmetries in the mid latitude ionosphere during the September 7–8, 2017 storm: Multi instrument observations. *Journal of Geophysical Research: Space Physics*, 126(4), e28829. https://doi.org/10.1029/2020JA028829
- Xiong, C., Stolle, C., Lühr, H., Park, J., Fejer, B. G., & Kervalishvili, G. N. (2016). Scale analysis of equatorial plasma irregularities derived from Swarm constellation. Earth Planets and Space, 68(1), 121. https://doi.org/10.1186/s40623-016-0502-5
- Yeh, H. C., & Foster, J. C. (1990). Storm tide heavy ion outflow at mid-latitude. Journal of Geophysical Research, 95(A6), 7881–7891. https://doi.org/10.1029/JA095iA06p07881
- Zakharenkova, I., & Cherniak, I. (2020). When plasma streams tie up equatorial plasma irregularities with auroral ones. Space Weather, 18(2), e02375. https://doi.org/10.1029/2019SW002375
- Zhai, C., Cai, X., Wang, W., Coster, A., Qian, L., Solomon, S. C., et al. (2023). Mid-latitude ionospheric response to a weak geomagnetic activity event during solar minimum. *Journal of Geophysical Research: Space Physics*, 128(1), e2022JA030908. https://doi.org/10.1029/2022JA030908
- Zhang, S.-R., & Aa, E. (2021). Ionospheric electron density large gradients at midlatitudes. In Y. Nishimura, O. Verkhoglyadova, Y. Deng, & S.-R. Zhang (Eds.), Cross-scale coupling and energy transfer in the magnetosphere-ionosphere-thermosphere system (pp. 175–193). Elsevier.
- Zhang, S.-R., Erickson, P. J., Coster, A. J., Rideout, W., Vierinen, J., Jonah, O., & Goncharenko, L. P. (2019). Subauroral and polar traveling ionospheric disturbances during the 7-9 September 2017 storms. Space Weather, 17(12), 1748–1764. https://doi.org/10.1029/2019SW002325
- Zhang, S.-R., Nishimura, Y., Erickson, P. J., Aa, E., Kil, H., Deng, Y., et al. (2022). Traveling ionospheric disturbances in the vicinity of stormenhanced density at midlatitudes. *Journal of Geophysical Research: Space Physics*, 127(8), e30429. https://doi.org/10.1029/2022JA030429
- Zhang, Y., Paxton, L. J., Morrison, D., Wolven, B., Kil, H., Meng, C. I., et al. (2004). O/N<sub>2</sub> changes during 1-4 October 2002 storms: IMAGE SI-13 and TIMED/GUVI observations. *Journal of Geophysical Research*, 109(A10), A10308. https://doi.org/10.1029/2004JA010441
- Zou, S., Moldwin, M. B., Ridley, A. J., Nicolls, M. J., Coster, A. J., Thomas, E. G., & Ruohoniemi, J. M. (2014). On the generation/decay of the storm-enhanced density plumes: Role of the convection flow and field-aligned ion flow. *Journal of Geophysical Research: Space Physics*, 119(10), 8543–8559. https://doi.org/10.1002/2014JA020408
- Zou, S., Ridley, A. J., Moldwin, M. B., Nicolls, M. J., Coster, A. J., Thomas, E. G., & Ruohoniemi, J. M. (2013). Multi-instrument observations of SED during 24-25 October 2011 storm: Implications for SED formation processes. *Journal of Geophysical Research: Space Physics*, 118(12), 7798–7809. https://doi.org/10.1002/2013JA018860

AA ET AL. 18 of 18